Fluid-induced disturbance of the monazite Th–Pb chronometer: In situ dating and element mapping in pegmatites from the…

Article *in* Chemical Geology · April 2009

DOI: 10.1016/j.chemgeo.2008.10.025

CITATIONS
62

READS
130

9 authors, including:

Valérie Bosse
Université Blaise Pascal - Clermont-Ferrand II
49 PUBLICATIONS **651** CITATIONS
SEE PROFILE

Philippe Boulvais
Université de Rennes 1
164 PUBLICATIONS **1,002** CITATIONS
SEE PROFILE

Gilles Ruffet
French National Centre for Scientific Research
163 PUBLICATIONS **2,658** CITATIONS
SEE PROFILE

Z. Cherneva
Sofia University "St. Kliment Ohridski"
35 PUBLICATIONS **294** CITATIONS
SEE PROFILE

Chemical Geology 261 (2009) 286–302

Contents lists available at ScienceDirect

Chemical Geology

journal homepage: www.elsevier.com/locate/chemgeo

Fluid-induced disturbance of the monazite Th–Pb chronometer: In situ dating and element mapping in pegmatites from the Rhodope (Greece, Bulgaria)

V. Bosse [a,*], P. Boulvais [b], P. Gautier [b], M. Tiepolo [c], G. Ruffet [b], J.L. Devidal [a], Z. Cherneva [d], I. Gerdjikov [d], J.L. Paquette [a]

[a] Laboratoire Magmas et Volcans, Université Blaise Pascal, UMR 6524 CNRS, Observatoire de Physique du Globe de Clermont Ferrand, France
[b] Geosciences Rennes, Université Rennes 1, UMR 6118 CNRS, France
[c] CNR — Istituto di Geoscienze e Georisorse, University of Pavia, Italy
[d] Department of Mineralogy, Petrology and Ore Geology, University of Sofia, Bulgaria

ARTICLE INFO

Article history:
Accepted 19 October 2008

Keywords:
Monazite
U–Th–Pb geochronology
LA-ICPMS
Oxygen isotopes
^{39}Ar–^{40}Ar
Rhodope

ABSTRACT

The monazite Th–Pb chronometer is widely used in a variety of geological contexts but may be affected by interaction with fluids. In the central part of the Rhodope Massif (Greece, Bulgaria), synfolial pegmatite veins were emplaced within two major synmetamorphic shear zones. In the Chepelare shear zone (CZS), which displays no evidence of post-metamorphic fluid flow, consistent monazite Th–Pb ages of ~36 Ma are interpreted as dating vein emplacement. Higher in the metamorphic pile, zircon and monazite give U–Th–Pb ages of ~42 Ma for vein emplacement. In the Nestos Shear Zone (NSZ) pegmatites show evidence of post-emplacement interaction with fluids during greenschist facies ductile deformation. Evidence for this includes the precipitation of calcite in microscale tension gashes within feldspar porphyroclasts, and the oxygen isotope disequilibrium between quartz and feldspar. Aqueous carbonic fluids deriving from carbonate lithologies in the footwall of the NSZ are identifiable in the pegmatites by the high $\delta^{18}O$ value of quartz (up to 21.8‰) and the presence of calcium in calcite veinlets. In these samples, some of the monazite grains show large intragrain scattering of Th–Pb age spanning up to ~12 Ma, with intergrain scattering reaching ~16 Ma (from ~39 to ~55 Ma). Within individual grains, age domains correlate with chemical heterogeneities, and some show a characteristic Ca-excess. These chemical and isotopic alterations are interpreted to be caused by interaction with fluids derived from carbonate lithologies. Complementary U–Pb data on zircons from the NSZ pegmatites yield mostly Mesozoic ages related to an older metamorphic cycle, and an age of ~48 Ma for one grain with typical magmatic zoning. The Th–Pb ages of 49.3 ± 1.6 to 54.9 ± 1.7 Ma probably relate to the emplacement of the pegmatites. The spread of younger Th–Pb ages (from 38.6 ± 1.1 to 46.2 ± 1.6 Ma) probably reflects the period of fluid circulation during progressive cooling to greenschist facies conditions, or variable perturbations of the monazite isotope system during fluid-assisted greenschist facies deformation. This is consistent with ^{39}Ar–^{40}Ar mica ages of ~32 to 34 Ma, interpreted as a tighter constraint for the timing of the greenschist facies metamorphism. This study illustrates the capacity of monazite to record distinct events in a single rock and highlights the need for identifying the potential involvement of fluids in order to interpret monazite ages.

1. Introduction

Monazite [(Ce, La, Nd, Th) PO_4] occurs as an accessory mineral in many metamorphic and magmatic rocks, and is thus extensively used for dating crustal processes. The development of in situ methods to analyze isotopes and chemistry has enabled us to examine the behaviour of the monazite Th–Pb and U–Pb chronometers in various environments (e.g. Poitrasson et al., 2000; Catlos et al., 2002; Goncalves et al., 2005; Pyle et al., 2005; Jercinovic and Williams, 2005; Rasmussen et al., 2006; Hinchey et al., 2007; McFarlane and McCulloch, 2007; Williams et al., 2007; Di Vincenzo et al., 2007). Other studies have pointed out that the diffusion rate of many elements, especially Pb, is very low in monazite (Smith and Giletti, 1997; Cherniak et al., 2004; Seydoux-Guillaume et al., 2002; Gardés et al., 2006). Thus, in principle, monazite should be particularly adapted to record various stages during a sequence of high-temperature geological events.

Monazite often displays distinct compositional and age domains together with complex chemical zoning patterns (Zhu and O'Nions,

* Corresponding author.
E-mail addresses: V.Bosse@opgc.univ-bpclermont.fr (V. Bosse), Philippe.Boulvais@univ-rennes1.fr (P. Boulvais), Pierre.Gautier@univ-rennes1.fr (P. Gautier), tiepolo@crystal.unipv.it (M. Tiepolo), J.L.Devidal@opgc.univ-bpclermont.fr (J.L. Devidal), cherneva@gea.uni-sofia.bg (Z. Cherneva), janko@gea.uni-sofia.bg (I. Gerdjikov), J.L.Paquette@opgc.univ-bpclermont.fr (J.L. Paquette).

0009-2541/$ – see front matter © 2008 Elsevier B.V. All rights reserved.
doi:10.1016/j.chemgeo.2008.10.025

1999a,b; Crowley and Ghent, 1999; Foster et al., 2000, 2002; Catlos et al., 2002; Kohn et al., 2005; Rasmussen et al., 2006; McFarlane and McCulloch, 2007; Hinchey et al., 2007). In some cases, these chemical patterns are associated with geologically meaningless ages (e.g., Seydoux-Guillaume et al., 2003). Fluid-assisted recrystallization constitutes an efficient way to reset the monazite chronometers under experimental conditions (Seydoux-Guillaume et al., 2002). In natural systems, Poitrasson et al. (1996, 2000) have described the behaviour of monazite during fluid–rock interaction processes that are classically observed within granitic rocks (chloritisation, greisenization, sericitization). They showed that Th–Pb and U–Pb systematics can be highly disturbed but may ultimately provide meaningful magmatic or fluid-alteration ages.

This study concerns monazite grains from synfolial pegmatite veins from the Rhodope Massif (northern Greece, Bulgaria). These rocks were emplaced within two high-grade shear zones several kilometers thick, classically described as Alpine synmetamorphic thrusts. Available geochronological data show that at least some of the rocks embedded in these shear zones experienced two major metamorphic cycles during Alpine orogenesis, with an apparent time gap of ~100 Ma in between. Careful investigation is thus needed to assess the exact meaning of new geochronological data. The two shear zones exhibit many characteristics in common, but differ strikingly in terms of footwall lithology; in one case it is carbonate-dominated, and in the other gneiss-dominated. Another difference is that deformation along the shear zone involving carbonates persisted during cooling down to greenschist facies conditions. Thrusting is commonly associated with dehydration–decarbonation of buried material, giving rise to large amounts of fluids that preferentially migrate into the hangingwall along high-permeability shear zones. Therefore, contrasting chemical signatures of fluids are expected between the two shear zones, probably with distinct chemical and isotopic evolution of their respective monazite grains. Moreover, because even low-temperature fluid circulation is capable of affecting monazite (Teufel and Heinrich, 1997; Hawkins and Bowring, 1997; Townsend et al., 2000), the influence of fluids on the monazite U–Th–Pb chronometer is expected to be more pronounced in the case of a shear zone that remained active during cooling to greenschist facies conditions.

This study presents electron microprobe analyses (in-situ analysis and element mapping) and back-scattered electron (BSE) imaging of monazite crystals separated from four pegmatite samples, together with in-situ Th–Pb dating by laser ablation-inductive coupled plasma mass spectrometry (LA-ICPMS). Oxygen isotope analyses performed on quartz and feldspar enable fluid–rock interactions within the pegmatites to be identified. ^{39}Ar–^{40}Ar dating of micas and U–Pb dates in zircon grains from the same samples provide additional and helpful constraints on the geological significance of the measured Th–Pb ages in monazite. In the light of these results, the alterations to the chemical and isotope systems of monazite during fluid-assisted greenschist facies deformation is discussed.

2. Geological setting

2.1. Tectono-metamorphic setting

The Rhodope Massif is a large crystalline complex lying in the northern part of the Aegean domain, straddling the border between Greece and Bulgaria (Fig. 1). It occupies a central position in the Alpine belt, between the southwest-verging Hellenides and the north-verging Balkanides. The massif mostly consists of high-grade metamorphic rocks and granitoids and represents the exhumed metamorphic core of the Alpine orogen. The precise timing of Alpine tectono-metamorphic events remains poorly known for much of the massif, available geochronological data suggesting a complex metamorphic evolution spanning Jurassic to late Cenozoic times (e.g., Krohe and Mposkos, 2002; Liati, 2005; Cherneva and Georgieva, 2005; Bonev et al., 2006).

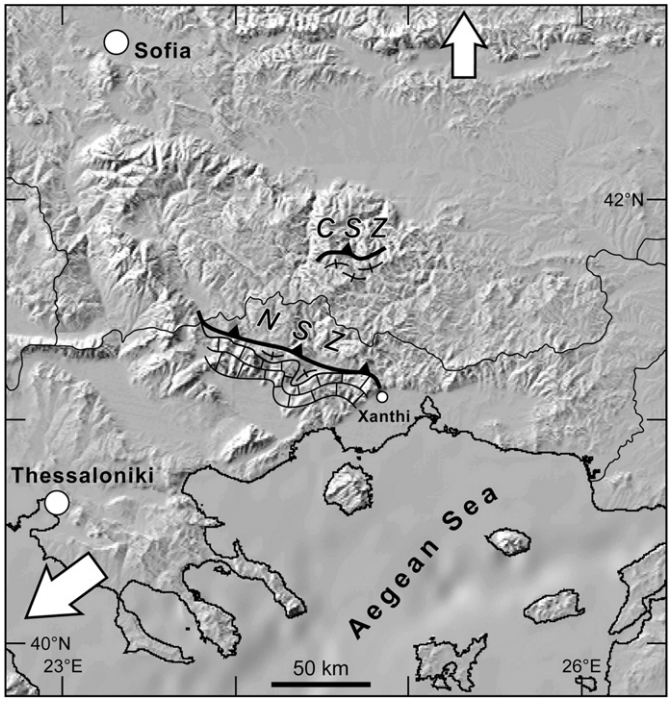

Fig. 1. Topographic map of the northern Aegean domain centered on the Rhodope Massif, with the locations of the two main shear zones (CSZ, Chepelare Shear Zone; NSZ, Nestos Shear Zone). The footwall of the CSZ consists of orthogneisses while that of the NSZ is dominated by carbonates. The arrows indicate the vergence of Alpine thrusting in the Balkanides, to the north, and the Hellenides, to the southwest.

This study focuses on two major synmetamorphic shear zones located in the central part of the Rhodope Massif (Fig. 1). The Nestos Shear Zone (NSZ) is exposed in Greece and was first described in the 1980s (Papanikolaou and Panagopoulos, 1981; Ivanov, 1981; Zachos and Dimadis, 1983). The Chepelare Shear Zone (CSZ) is exposed in Bulgaria and was first reported by Burg et al. (1990). Both shear zones dip northward and consist of a >1 km-thick pile of mylonites displaying top-to-southwest shear sense criteria (e.g., Kilias and Mountrakis, 1990; Dimov et al., 1996; Barr et al., 1999). According to these authors as well as others (e.g., Dinter, 1998; Krohe and Mposkos, 2002), the two shear zones represent synmetamorphic thrusts. For Ricou et al. (1998), they represent main structures which accommodated Alpine convergence in the innermost part of the Hellenides.

The hangingwall unit of both shear zones is composed mainly of migmatites developed at the expense of orthogneisses and minor paragneisses in the two localities. In contrast, the footwall unit differs in each case. The footwall of the NSZ exposes a thick pile of marbles. In the area of Xanthi, where the samples of this study come from, marbles are at least 1.5 km thick and form the immediate footwall of the main tectonic contact associated with the NSZ (Fig. 1). The footwall of the CSZ exposes a pile of mesocratic to felsic orthogneisses at least 3 km thick. These orthogneisses are overlain by a <1 km-thick layered package of mylonitic gneisses, marbles, micaschists and amphibolites, known as the 'Chepelare Formation'. According to Gerdjikov et al. (2003), the Chepelare Formation constitutes the hangingwall immediately above the main tectonic contact associated with the CSZ.

Both the NSZ and the CSZ represent high-grade shear zones, however deformation along the NSZ persisted at lower temperature conditions. Our observations of the NSZ in the area north of Xanthi indicate that top-to-SW shearing at lower levels of the hangingwall unit occurred first at higher amphibolite facies conditions, with concurrent anatexis, and persisted during cooling down to greenschist facies conditions, at which stage deformation became more localized

within discrete shear zones (see also Kilias and Mountrakis, 1990; Krohe and Mposkos, 2002). In contrast, shearing along the CSZ first developed during the anatexis of felsic gneisses in both the hanging-wall and footwall units, but ceased before the rocks cooled to greenschist facies conditions (Dimov et al., 1996; Gerdjikov et al., 2003).

2.2. Previous geochronology

Geochronological data on rocks embedded in the NSZ have yielded three broad age groups. The first group consists of Proterozoic to Early Triassic U–Pb and Pb–Pb zircon ages, inherited from various protoliths (Liati, 2005; Turpaud, 2006). The second group, at ~150–140 Ma, is represented by U–Pb SHRIMP ages on metamorphic rims of zircon (Liati, 2005) and U–Th–Pb LA-ICPMS ages on monazite (Bosse et al., 2006) from garnet–kyanite metapelites near Xanthi. To date, this lithology has yielded the most convincing evidence of a relict ultrahigh-pressure metamorphic event in this part of the Rhodope metamorphic pile (Mposkos and Kostopoulos, 2001; Perraki et al., 2006). From the same lithology, Reischmann and Kostopoulos (2002) reported microprobe monazite ages clustering around 185 and 165 Ma, and a Sm–Nd garnet — whole rock age of ~140 Ma. Orthogneiss higher up in the northwards-dipping metamorphic pile have yielded U–Pb and Pb–Pb zircon ages in the range of ~165 to 135 Ma; this is interpreted as dating the magmatic protoliths (Turpaud, 2006). K–Ar and Rb–Sr chronometers essentially yield the third group of ages, from ~50 to 35 Ma. From metamorphic rocks within the NSZ near Xanthi, Liati (1986) obtained K–Ar hornblende ages of ~47–37 Ma, and K–Ar muscovite and biotite ages of ~36–35 Ma. From the garnet–kyanite metapelites, Reischmann and Kostopoulos (2002) obtained Rb–Sr mica — whole rock ages of ~37 Ma for muscovite and ~34 Ma for biotite. At higher levels of the metamorphic pile, Liati and Gebauer (1999) obtained U–Pb SHRIMP zircon ages of ~45 Ma from a synfolial quartz vein and ~36 Ma from a pegmatite which was reportedly undeformed. About 60 km further west along the strike of the NSZ, from lower in the hangingwall unit, U–Pb ages of ~51 Ma and ~40 Ma were obtained on metamorphic rims of zircons from an amphibolitized eclogite and a migmatitic leucosome, respectively (Liati, 2005).

Geochronological data are scarce for the CSZ, but the same three age groups exist. Arkadakskiy et al. (2000) reported monazite and zircon U–Pb ages of about 37 Ma from diatexites near the roof of the shear zone (see also Cherneva and Georgieva, 2005). In the same rocks inherited zircons have yielded Carboniferous ages, which are presumed to be remnants from a Hercynian protolith. Bosse et al. (2006) reported monazite LA-ICPMS U–Th–Pb ages of about 140 Ma from a garnet–kyanite metapelite within the Chepelare Formation.

This summary shows that rocks embedded in both the NSZ and the CSZ bear witness to the imprint of at least two major Alpine metamorphic cycles, one in the mid-Mesozoic, the other in the mid-Cenozoic, with an apparent age gap of about 100 Ma (see also Liati, 2005; Bosse et al., 2006).

3. Field relations and sample description

The pegmatites in this study were collected within the NSZ (4.5 km north–northwest of Xanthi, along the Xanthi River; samples P04-13, P04-26 and P04-27) and the CSZ (1 km east of Chepelare; sample P04-64). In addition, P04-56 comes from above the CSZ, higher in the northwards-dipping metamorphic pile (32 km northwest of Chepelare, along the Vacha valley).

The samples from the NSZ lie at lower levels of the hangingwall unit, structurally about 1 km above the contact, with thick marbles in the footwall unit. P04-26 and P04-27 were taken from two pegmatite veins only 2 m apart. P04-13 is from another vein about 300 m further east, at a roughly equivalent structural level. Pegmatite P04-13 crosscuts the layering of the host metapelites. Vein thickness is irregular (0–40 cm) as a result of boudinage (Fig. 2a). The boudins' internal foliation, of variable intensity, is concordant with that of the host rocks. Among the host metapelites there are several layers (up to 10 cm thick), which are more heterogeneous, containing quartz–feldspath segregations, biotite-rich selvages and centimeter-sized garnets, giving the rock a typical migmatitic appearance (Fig. 2a). A progressive lateral transition was observed between one such layer and a boudin of pegmatite P04-13, the margins of which also show large garnets and a diffuse contact with the host metapelites (Fig. 2b). We interpret these features as indicating that the pegmatite originated from the anatexis of the host metapelites. P04-27 is also a pegmatite vein of irregular thickness (up to 30 cm) with an internal foliation paralleling that of the hosting biotite–garnet gneisses. It has uneven boundaries, while the host gneisses contain randomly distributed cm-thick synfolial quartz–feldspar segregations (Fig. 2c). The contact between the vein and the segregations is transitional. The garnet also becomes larger and more abundant closer to the vein. These features suggest that this pegmatite, too, originated from anatexis of its host gneisses. Close to P04-27, P04-26 samples a series of ~5 cm-thick felsic veins which crosscut the foliation and mm-scale compositional layering of hosting amphibolites at a low angle (Fig. 2d). The amphibolites lie concordantly on the above mentioned biotite–garnet gneisses. The markedly diffuse contacts between felsic veins and host amphibolites indicate that the veins were emplaced at high-grade conditions. They also possibly originated from anatexis of the amphibolites.

P04-13 and P04-27, the two samples of the NSZ from which monazite was extracted, show similar structures under the microscope. The most striking feature is the difference in grain size, and the amount and style of deformation between quartz and feldspar. Quartz commonly appears as polycrystalline aggregates of small ($\leq$0.3 mm) elongate grains with a pronounced preferred orientation (Fig. 2e). Individual grains display undulose extinction and subgrain formation. This shows an extensive dynamic recrystallization of the quartz. In contrast, feldspars most commonly appear as large (up to several centimeters) crystals that are not significantly strained. Nevertheless, feldspar aggregates with a seriate subpolygonal texture also occur as discontinuous mantles around porphyroclasts. The largest clasts also show this texture within discrete ~0.5–2 mm-wide deformation bands. In addition, feldspars are frequently cut by a set of parallel fractures that do not extend through adjacent quartz aggregates (Fig. 2f), showing that the feldspars showed a brittle response, while that of the quartz was plastic. Occasionally the quartz grain shape fabric warps around the sharp edges of feldspar clasts, illustrating the contrast in competency between the two minerals (Fig. 2e). Quartz aggregates between felspar microboudins, or in strain shadows beside feldspar clasts, are composed of larger grains with no, or only a weak, preferred orientation, which also reflects the greater strength of feldspar. The fractures inside feldspars host calcite, feldspar/quartz (frequently as pallisadic euhedral grains) and fibrous muscovite, thus providing evidence for the precipitation of new minerals from a fluid. These fractures are oriented at right angles to the external quartz fabric, suggesting that they represent microscale tension gashes. In P04-27, primary biotite is partially replaced by finer-grained chlorite, and the largest biotite flakes are frequently kinked. In P04-13, the large muscovite flakes have been deformed into curves.

The above features indicate that at least part of the deformation within the two pegmatites occurred at greenschist facies conditions (e.g., Simpson, 1985). Additional microstructural observations suggest that deformation started at higher-grade conditions. Further agreement with this latter view is that the pegmatite veins are heterogeneously, but pervasively, deformed and show no sharp strain gradient. This is more typical for quartzofeldspathic rocks having been strained at an early stage, at temperatures of above 500–550 °C (Gapais, 1989).

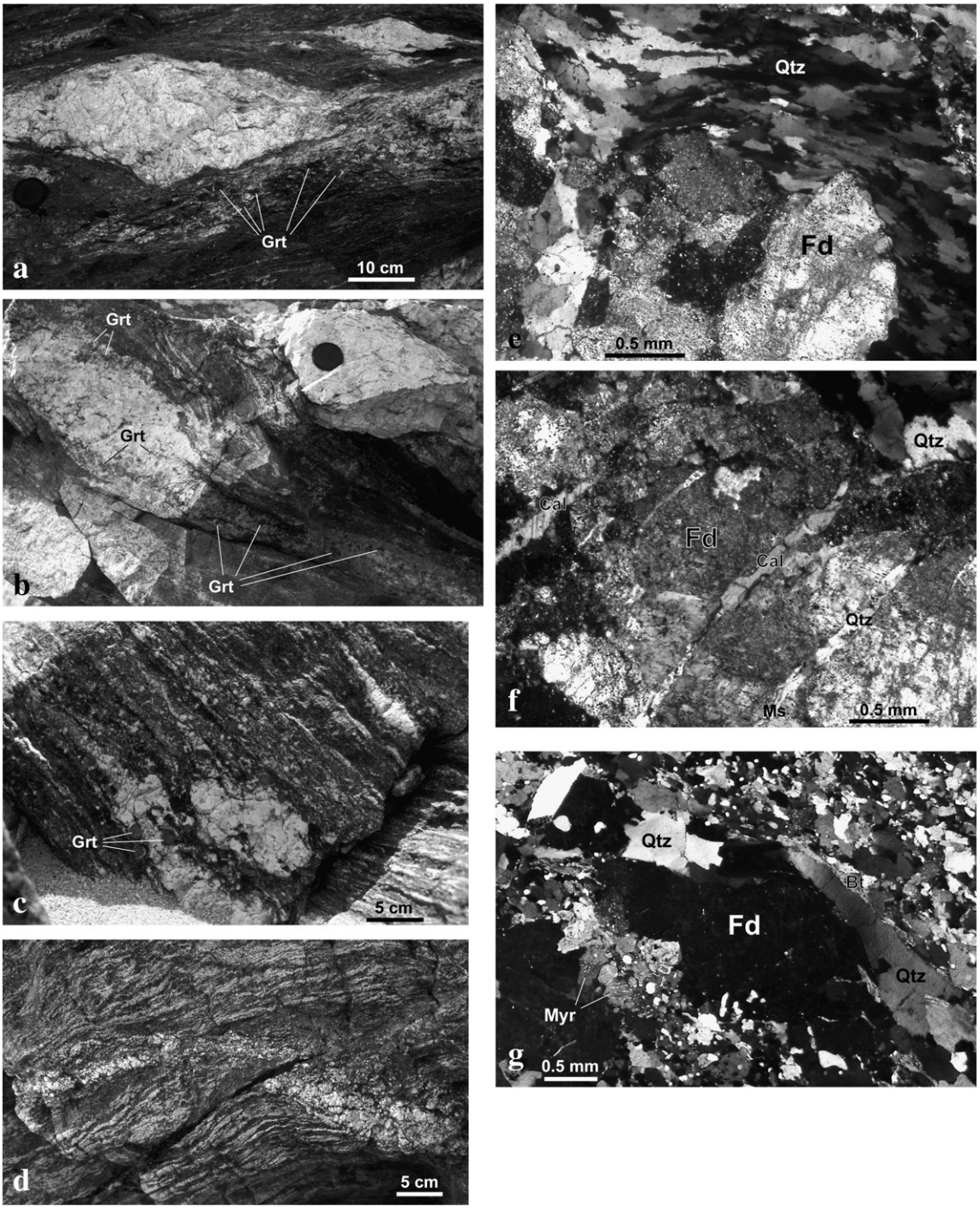

Fig. 2. (a) and (b) Field views of pegmatite P04-13. In (a) the vein is dismembered due to boudinaging. The left-dipping leucocratic layer next to the main boudin contains centimetric garnets ('Grt') and represents a metapelitic horizon which has undergone partial melting. The opposite flank of the outcrop, in (b), shows a progressive lateral transition between one such horizon and another boudin of the pegmatite. (c) Field view of pegmatite P04-27, hosted by garnet–biotite gneisses with unevenly distributed quartz–feldspar segregations. Larger garnets ('Grt') occur on the margins of the pegmatite. (d) Field view of pegmatite P04-26. (e) and (f) Photomicrographs of sample P04-13. (g) Photomicrograph of sample P04-64 ('Myr' denotes myrmekites). See the text for a description of microstructures.

Sample P04-64, from the CSZ, was taken from a pegmatite vein within the 'Chepelare Formation', in the lowest part of the hanging-wall unit (cf. Gerdjikov et al., 2003). The vein is of almost constant thickness (20 cm) for several meters and is concordant with the cm-scale compositional layering and mylonitic foliation of host felsic gneisses, amphibolites and calcsilicates. Its internal pervasive foliation has the same orientation. When viewed under the microscope (Fig. 2g), much of the rock shows a mixture of feldspars and quartz which form a fine-grained subpolygonal texture which is vermicular in places. This texture alternates with quartz ribbons containing large grains with deeply indented boundaries, and with discontinuous layers of synfolial biotite partially replaced by a mimetic overgrowth of chlorite. K-feldspar porphyroclasts are relatively rare and show myrmekitic replacement lobes along their margins paralleling the foliation. These features document high amounts of strain accumulated at amphibolite facies or higher-grade conditions (e.g., Simpson, 1985) and show no evidence of subsequent deformation during greenschist facies metamorphism.

Sample P04-56, from above the CSZ, was taken from a series of ~10–50 cm-thick felsic veins crosscutting the foliation of hosting amphibolites at low to moderate angles. The veins show a pervasive high-strain foliation parallel to their margins, with ultramylonitic bands occurring preferentially along the margins. The geometry of the veins indicates that they were emplaced along mesoscale shear bands associated with a top-to-WNW shearing event that is kinematically distinct from the top-to-SW shearing event recorded throughout the CSZ. For convenience, P04-56 and P04-64 will be treated together, in the following discussion, as samples 'from the CSZ'. However, as we suggest in the discussion, the obtained ages should be interpreted separately.

4. Analytical procedures

4.1. Mineral separation

Zircon is very abundant whereas monazite, though present in all samples (except in P04-26), is scarce. Only 10 to 20 grains of monazite were found in 5 to 10 kg of rock. Thus, LA-ICPMS and microprobe analyses could not be carried out on thin sections. Monazite and zircon were obtained by crushing then sieving through heavy liquids and Frantz magnetic separators. From the five samples described in Section 3, 18 grains of monazite and 36 grains of zircon were extracted, mounted on epoxy resin and polished using 0.25 µm diamond paste. The size of the monazite grains typically ranges from 100 to 300 µm (Figs. 3 and 4). Most grains show irregular or rounded–subhedral shapes; euhedral grains are rare, e.g. in sample P04-64. Many grains also contain fractures. We see no intra-grain spatial correlation between the distribution of elements and the occurrence of fractures, therefore most of these fractures probably developed during the polishing procedure.

Single grains of muscovite and biotite used for the ^{39}Ar–^{40}Ar experiments were handpicked under a binocular microscope from 0.25–1.0 mm fractions of crushed rock samples.

4.2. EMP analyses

Quantitative analysis and X-ray mapping of monazite were carried out using a Cameca PC-controlled-SX 100 type (LMV, Clermont-

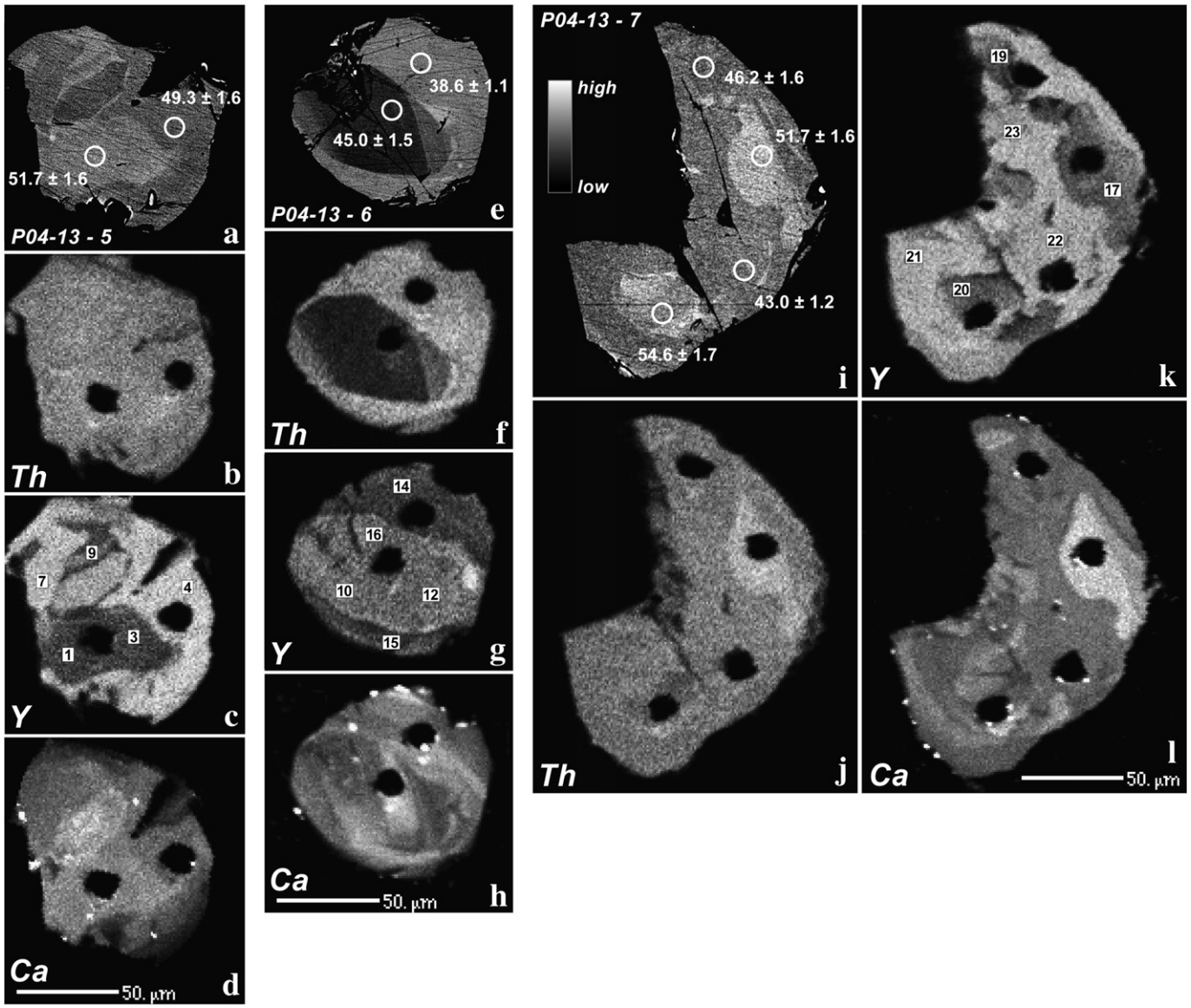

Fig. 3. BSE images and X-ray maps of monazite from samples of the NSZ: grains P04-13-5 (a to d), P04-13-6 (e to h) P04-13-7 (i to l), P04-13-8 (m to p), P04-13-9 (q to t) and P04-27 (u to x). BSE images show the location of ICPMS laser ablation pits (10 µm) and their corresponding ^{232}Th–^{208}Pb ages (2σ level). Numbers shown on Y maps correspond to microprobe analyses reported in Tables 1a, b, c, d.

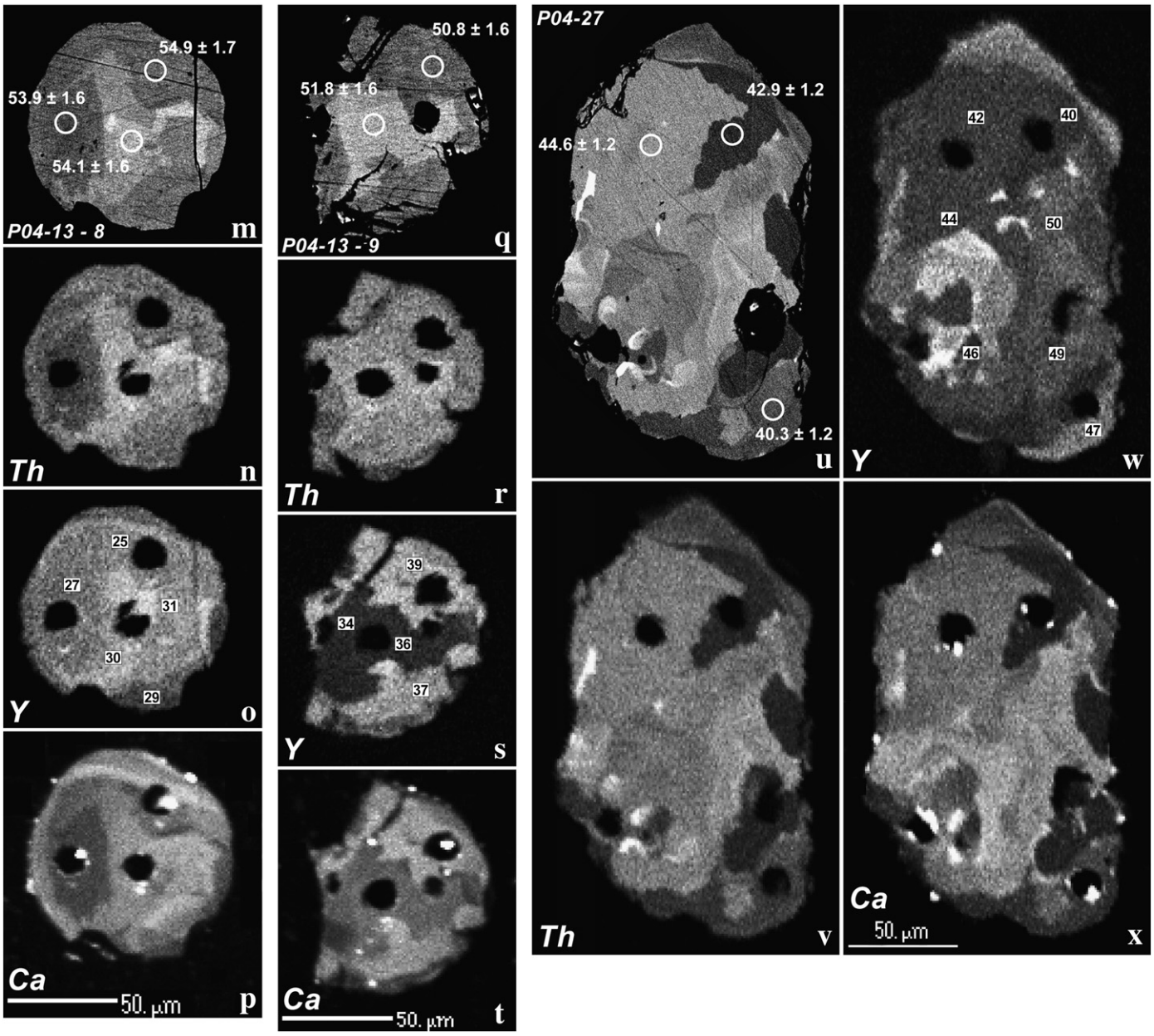

Fig. 3 (*continued*).

Ferrand). During analysis of major and trace elements, an accelerating voltage of 15 kV, beam current of 100 nA and peak counting time 10 to 25 s. X-ray lines were used, and background offsets and standards were derived from the earlier study of Montel et al. (1996). Compositional images were performed at 15 kV and 200 nA, using a focused beam either in beam or stage scanning mode, depending on map dimensions. The dwell time per pixel was set to 100 ms and the pixel step to 1 µm. The selected X-ray lines were Ca*Kα*, Y*Lα*, La*Lα*, Th*Mα* and U*Mβ*. Selected quantitative electron microprobe analyses and La, Y, U and Th elemental mapping are shown in Fig. 4 and Tables 1a, b, c, d.

4.3. LA-ICPMS U–Th–Pb analyses

U–Th–Pb analyses on monazite and zircon were carried out by Laser Ablation-ICPMS at the CNR-Istituto di Geoscienze e Georisorse-Unità di Pavia. Analytical procedures are reported in detail in Tiepolo (2003) andPaquette and Tiepolo (2007). The LA-ICPMS instrument couples an Argon Fluoride 193 nm excimer laser (type GeoLas 102 from MicroLas) with a sector field ICP-MS (type Element I from ThermoFinnigan). The spot size was 10 µm in diameter for the monazites, 35 µm for the NSZ zircons and 20 µm for the CSZ zircons, with an energy density of 12 J cm^{-2} and a repetition rate of 3 Hz. Time resolved signals were carefully inspected to verify the presence of perturbations related to inclusions, fractures, mixing of different age domains or common Pb. Laser induced elemental fractionation and mass bias were corrected using a matrix matched external standard (Moacir monazite: Cruz et al., 1996, Seydoux-Guillaume et al., 2002a,b; Zircon 91500: Wiedenbeck et al., 1995). To ensure the efficient correction of fractionation effects, external standards and unknowns were integrated over the same time intervals (external standards analyses, Table 4 in the Appendix, are available as an electronic supplement). Data reduction was carried out with GLITTER software developed by van Achterbergh et al. (2001) and in order to estimate better the uncertainty affecting the $^{206}Pb/^{238}U$, $^{207}Pb/^{235}U$ and $^{208}Pb/^{232}Th$ isotope ratios, the individual uncertainties given by GLITTER® for the isotope ratios were propagated relative to the respective external reproducibility of the standard (Moacir: 14 values and 91500: 40 values). After this error propagation each analysis remains accurate

within the quoted errors (Paquette and Tiepolo, 2007). All the ages are presented at the 2σ level. Only ^{232}Th–^{208}Pb ages are used for monazite because:

1) ^{232}Th is highly abundant and enables small spots to be performed by laser ablation.
2) U decay series could be in disequilibrium in young monazites (Schärer, 1984;), resulting in overestimated ^{206}Pb/^{238}U ages. Secular equilibrium among the intermediate decay products of ^{232}Th occurs after about 30 years, so it seems reasonable to assume that initial ^{208}Pb is absent.
3) ^{232}Th is so abundant that ^{208}Pb originating from common Pb is negligible compared to radiogenic ^{208}Pb.

4.4. ^{39}Ar–^{40}Ar data

Selected grains of muscovite (samples P04-13 and P04-64) and biotite (sample P04-27) were wrapped in Al foil to form small packets (11 × 11 mm) that were stacked up to form a pile into which fluence monitors were inserted every 10 samples. Irradiation was performed at the McMaster reactor (Hamilton, Canada). Irradiation lasted 40 h (total fluence of 2.4×10^{18} n cm^{-2}), and the irradiation standard was sanidine TCR-2 (28.34 Ma; Renne et al., 1998). The sample arrangement within the irradiation allows us to monitor the flux gradient with an estimated precision as low as ±0.2%. The laser step-heating experiment on single grains was described by Ruffet et al. (1991, 1995). Blanks were performed routinely each first or third step, and

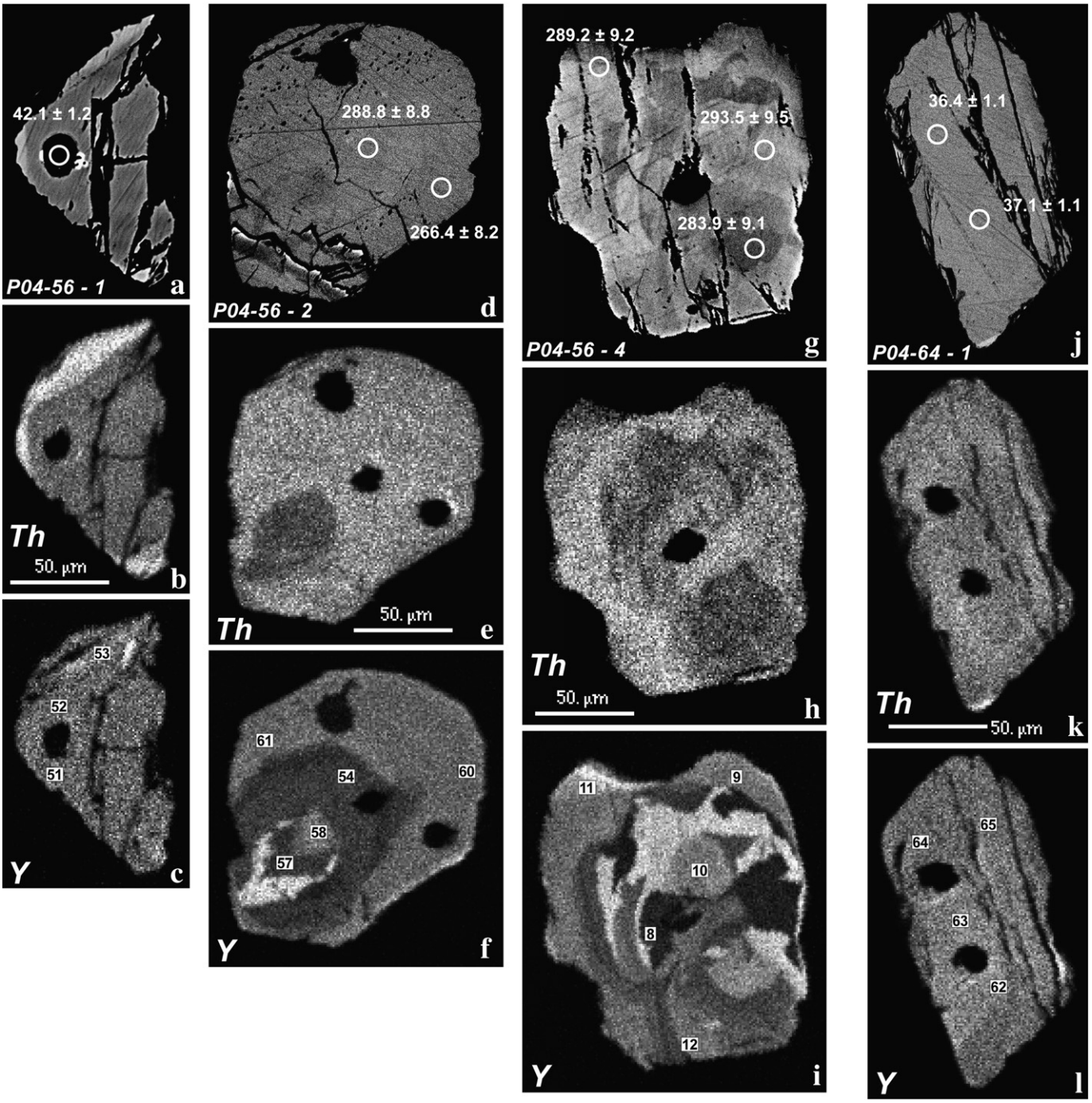

Fig. 4. BSE images and X-ray maps of monazite crystals from samples of the CSZ: grains P04-56-1 (a to c), P04-56-2 (d to f), P04-56-4 (g to i), P04-64-1 (j to l), P04-64-3 (m to o), P04-64-4 (p to r) and P04-64-5 (s to u). Same annotation as in Fig. 3.

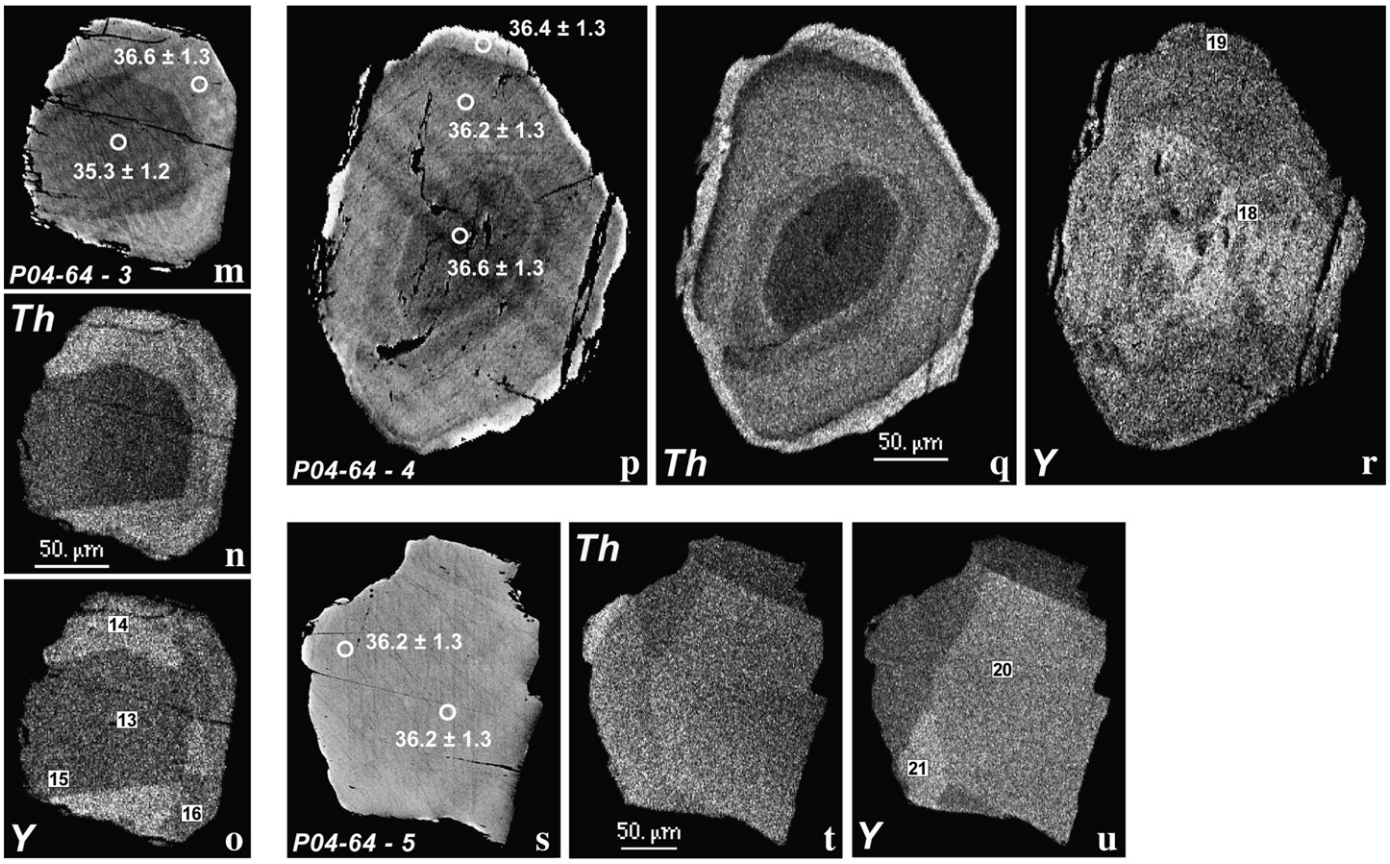

Fig. 4 (*continued*).

subtracted from subsequent sample gas fractions. All ages are displayed at the 1σ level.

4.5. Oxygen isotope analysis

Quartz (Qtz)–Feldspar (Fd) pairs were analyzed in Geosciences Rennes, Université de Rennes 1, France in the four pegmatite veins that yielded monazite ages (Table 3 and Fig. 9). Minerals were separated by handpicking and finely crushed in a boron carbide mortar. Powders were reacted with BrF_5 in Ni tubes at 680 °C overnight, following the method of Clayton and Mayeda (1963). The liberated O_2 was then converted to CO_2 by reaction with hot graphite. Isotopic compositions of this CO_2 were measured using a VG SIRA 10 triple collector mass spectrometer. During the analytical session, measurements of a NBS 28 quartz standard gave $\delta^{18}O = 9.34 \pm 0.09$ (1σ, $n = 14$). Analyses were normalized to NBS 28 ($\delta^{18}O = 9.60‰$) by adding 0.26‰ to the measured value. The long-term analytical uncertainty on measurements is about ± 0.15 (1σ).

5. Chemical and isotopic data in monazites

5.1. Monazite geochemistry and element mapping

Chemical compositions are reported in Tables 1a, b, c, d and Y, Th and Ca mapping of monazite grains are shown in Figs. 3 (NSZ) and 4 (CSZ). All grains belong to the most common species Monazite-(Ce) with compositions consistent with those published by Chang et al. (1998).

Table 1a
Electron microprobe analyses (%) of the NSZ monazite grains.

NSZ																
Sample	P04-13-5					P04-13-6					P04-13-7					
An. no.	1	3	4	7	9	10	12	14	15	16	17	19	20	21	22	23
SiO_2	0.1	0.1	0.1	0.1	0.1	0.2	0.3	0.4	0.4	0.1	0.3	0.3	0.2	0.2	0.3	0.3
CaO	2.3	2.4	2.2	2.3	2.4	1.3	1.1	1.4	1.4	1.3	2.2	2.0	1.9	1.7	1.8	1.8
P_2O_5	30.6	30.7	30.9	30.9	30.4	30.5	30.8	30.7	30.4	30.7	31.0	31.3	30.9	31.2	30.8	31.3
La_2O_3	14.3	13.8	13.9	13.5	13.9	16.3	16.2	15.6	15.6	16.7	13.0	13.5	12.2	13.0	12.9	12.5
Ce_2O_3	27.5	27.3	26.7	25.9	27.2	31.2	30.1	29.4	29.6	31.2	26.5	26.9	26.5	26.6	26.0	25.5
Pr_2O_3	2.3	2.4	2.3	2.3	2.4	2.6	2.6	2.5	2.5	2.5	2.4	2.5	2.4	2.3	2.4	2.4
Nd_2O_3	9.2	9.2	9.2	9.1	9.4	10.0	9.9	9.3	9.6	9.6	9.0	9.0	9.3	9.2	9.3	9.4
Sm_2O_3	1.3	1.6	1.4	1.4	1.4	1.2	1.2	1.2	1.2	1.1	1.5	1.3	1.8	1.4	1.7	1.7
Gd_2O_3	1.2	1.2	1.3	1.2	1.1	0.9	1.0	0.9	0.9	0.8	1.3	1.2	1.6	1.4	1.5	1.5
Y_2O_3	1.7	1.7	3.1	3.2	1.8	1.8	1.7	1.3	1.1	1.6	2.1	2.5	2.0	3.0	3.1	3.3
ThO_2	7.1	7.6	6.6	6.7	7.3	1.4	3.2	5.7	5.6	1.5	9.9	7.7	8.3	7.5	8.1	8.7
UO_2	0.7	0.6	1.0	1.1	0.8	0.5	0.4	0.3	0.4	0.4	0.4	0.7	1.1	0.3	0.3	0.4
Total	98.4	98.6	98.7	97.7	98.4	97.8	98.6	98.6	98.8	97.4	99.6	98.8	98.1	97.9	98.3	98.7
Ca/Th + U	1.4	1.4	1.3	1.4	1.4	3.3	1.4	1.1	1.1	3.1	1.0	1.1	0.9	1.0	1.0	1.0

Location of the sample P04-13: N41° 11,148′; E 24° 51,895′.

Table 1b
Electron microprobe analyses (%) of the NSZ monazite grains.

NSZ																
Sample	P04-13-8					P04-13-9				P04-27						
An. no.	25	27	29	30	31	34	36	37	39	40	42	44	46	47	49	50
SiO_2	0.5	0.6	0.7	1.0	1.2	0.8	0.8	0.3	0.4	0.5	1.6	1.2	0.7	1.0	0.4	1.3
CaO	1.3	0.8	0.8	1.1	1.2	1.0	1.1	1.3	1.1	0.9	1.2	1.3	1.0	0.9	0.9	1.3
P_2O_5	31.2	30.8	30.6	30.7	30.1	30.6	29.8	30.7	31.1	30.7	29.0	29.5	30.4	30.4	30.8	29.4
La_2O3	12.3	13.6	13.0	12.2	12.3	16.6	16.8	15.6	15.8	15.6	13.7	13.3	15.1	15.1	14.9	13.8
Ce_2O_3	27.3	28.9	29.2	26.9	26.0	30.5	30.2	29.3	29.9	30.6	28.2	27.9	31.1	29.9	30.7	27.8
Pr_2O_3	2.7	2.7	2.7	2.5	2.4	2.3	2.3	2.4	2.4	2.5	2.3	2.4	2.5	2.4	2.8	2.4
Nd_2O_3	10.0	10.4	10.8	9.8	9.6	9.1	8.7	8.7	8.8	10.0	9.1	8.5	9.9	8.6	10.3	8.7
Sm_2O_3	1.5	1.6	1.7	1.5	1.5	1.0	0.7	1.1	1.1	1.3	1.3	1.4	1.1	1.3	1.4	1.4
Gd_2O_3	1.4	1.2	1.2	1.4	1.4	0.4	0.5	1.0	0.9	0.7	0.7	1.2	0.6	0.8	0.8	1.0
Y_2O_3	2.8	2.6	1.9	3.3	3.0	0.4	0.4	1.6	1.1	0.5	0.6	1.5	0.4	1.0	0.7	0.8
ThO_2	6.7	5.1	6.0	7.8	9.4	7.2	7.9	6.7	6.2	5.8	11.7	10.7	7.2	7.8	5.3	10.9
UO_2	1.2	0.7	0.4	1.0	1.0	0.1	0.2	0.4	0.3	0.0	0.2	0.4	0.1	0.4	0.1	0.2
Total	98.9	98.9	99.0	99.2	99.1	99.9	99.3	99.1	99.0	99.1	99.5	99.3	100.3	99.7	99.2	98.8
Ca/Th + U	0.8	0.6	0.6	0.6	0.6	0.6	0.6	0.9	0.8	0.7	0.5	0.4	0.6	0.5	0.8	0.5

Location of the sample P04-27 (and P04-26): N 41°11,243; E 24° 51,582′.

In the NSZ (Tables 1a and b), monazites cover a large domain of compositions. REE, Y and U contents vary from one grain to another (Ce_2O_3: 25.5 to 31.2 wt.%, La_2O_3: 12.2 to 16.8 wt.%, Y_2O_3:0.4 to 3.3 wt.%, UO_2: 0.04 to 1.2 wt.%; Tables 1a and b). A special feature of monazites P04-13-5 and P04-13-7 (Fig. 3) is their high CaO content (2.4–2.6 wt. %), which correlates with the highest ThO_2 contents and with Ca/(Th + U) ≥ 1 (Table 1a). Monazite P04-13-6 displays a lower CaO content (1.1–1.4 wt.%) but since the Th content is very low (ThO_2: 1.4–5.6 wt.%), the Ca/(Th + U) ratio is as high as 3.3 (Table 1a). In contrast, P04-13-8, P04-13-9 and P04-27 have a lower CaO content (0.7–1.3 wt.%; Tab 1b) for similar, or higher, ThO_2 content (Ca/(Th + U) ≤ 0.9; Table 1b).

BSE images of the NSZ monazite show complex internal zoning patterns (Fig. 3) which correspond to distinct chemical domains, as shown by the Y, Th and Ca mapping. The domains are fairly large (at least 20 μm) and have sharply defined boundaries. Th zoning is generally patchy, but there is a clear tendency for Th to decrease toward the rims of the grains (Fig. 3b, j, n, r, v). In contrast, P04-13-6 shows concentric zoning (Fig. 3f) with a Th-poor core (1.4 wt.%) surrounded by a Th-rich rim (5.6 wt.%). Y-zoning generally mimics Th zoning either with direct (Fig. 3n and o) or, more frequently, inverse correlation (Fig. 3b and c, f and g, r and s), or even with both correlations in a single grain (Fig. 3j and k). P04-27 displays essentially distinct Th and Y patterns Fig. 3v and w). Ca zoning mimics Th zoning with direct (Fig. 3b and d, j and l, n and p, v and x) or, more rarely, inverse correlation (Fig. 3r and t). Again, P04-13-6 is different as no clear relation is found between Ca and Th or Y (Fig. 3f and h).

Most chemical variations observed in the NSZ monazite grains could be explained by brabantite ($2\ REE^{3+} = Th^{4+} + Ca^{2+}$) and, to a lower extent, huttonite ($REE^{3+} + P^{5+} = Th^{4+} + Si^{4+}$) exchanges. However, some grains from P04-13 show Ca contents which appear not to be balanced by the brabantite exchange (Fig. 5). Most monazite compositions follow a linear trend in the field of Ca − Th + U < 0 (Fig. 5), which illustrates the correlation of Th + U with Si, typical for huttonite exchange. Analyses with Ca − Th + U > 0 in grains P04-13-5, P04-13-6 and P04-13-7 indicate that Ca is involved in the brabantite exchange and other substitution schemes (REE, P; Chang et al., 1998; Williams et al., 2006).

Monazite grains from the CSZ (Fig. 4) display much more homogeneous compositions when compared to the NSZ monazite grains (Table 1c). The grains of sample P04-56 form two groups with distinct compositions (Table 1c). The first group is represented by P04-56-1, which shows an increase in Th (Fig. 4b) and Si, and a decrease in LREE, Ca and P from core to rim (Table 1c). The compositions of the second group, represented by P04-56-2, P04-56-3 (not shown in Table 1c) and P04-56-4 are much more homogeneous and differ strikingly from P04-56-1 (Table 1c). Despite this relative homogeneity, Y and Th display clear zoning patterns, concentric in P04-56-2 (Fig. 4e and f) or patchy in P04-56-4 (Fig. 4h and i). The grains from sample P04-64 have homogeneous chemical compositions (Table 1d). Th and Y mapping reveal concentric (Fig. 4n, q) to patchy (Fig. 4o, r, t, and u) zoning patterns or no zonation at all (Fig. 4k and l). Zonations, when present, correspond to the minimal compositional variations between grains (Table 1c).

Table 1c
Electron microprobe analyses (%) of the CSZ monazite grains.

CSZ													
Sample	P04-56-1			P04-56-2					P04-56-4				
An. no.	51	52	53	54	57	58	60	61	8	9	10	11	12
SiO_2	0.5	0.5	1.5	0.3	0.7	0.5	0.4	0.4	0.7	0.3	0.6	0.3	0.4
CaO	0.9	0.9	0.8	1.6	0.6	0.9	1.5	1.5	0.9	1.3	1.0	1.2	1.5
P_2O_5	30.6	30.7	28.9	31.0	30.3	30.4	30.5	30.7	30.1	30.3	30.1	30.4	30.7
La_2O_3	19.4	18.9	17.9	14.5	16.1	14.6	13.5	13.4	14.2	13.5	14.3	13.5	13.3
Ce_2O_3	31.6	31.5	30.4	28.8	30.6	30.0	28.3	27.7	29.0	28.3	29.3	28.2	27.5
Pr_2O_3	2.1	2.1	2.3	2.6	2.5	2.7	2.8	2.6	2.7	2.8	2.9	2.8	2.8
Nd_2O_3	7.4	7.2	7.6	9.4	9.9	10.1	10.3	9.9	10.7	10.9	10.3	10.5	10.4
Sm_2O_3	0.6	0.5	0.7	1.3	1.1	1.4	1.7	1.5	1.5	1.7	1.6	1.8	1.7
Gd_2O_3	0.4	0.4	0.4	1.0	0.7	1.0	1.1	1.1	0.8	1.2	1.0	1.2	1.1
Y_2O_3	0.4	0.4	0.4	0.6	0.7	1.1	1.0	1.0	0.8	1.1	1.2	1.1	0.8
ThO_2	4.9	5.2	7.8	8.2	5.5	5.9	7.9	7.8	7.0	6.8	6.8	6.9	8.5
UO_2	0.3	0.3	0.3	0.6	0.2	0.2	0.3	0.3	0.2	0.4	0.2	0.4	0.3
Total	99.0	98.6	98.9	99.9	98.8	98.9	99.2	97.9	98.5	98.5	99.2	98.4	99.0
Ca/Th + U	0.8	0.8	0.4	0.9	0.5	0.7	0.8	0.9	0.6	0.8	0.6	0.8	0.8

Location of the sample P04-56: N 41° 56,408′;E 24° 26,227′.

Table 1d
Electron microprobe analyses (%) of the CSZ monazite grains.

CSZ												
Sample	P04-64-1				P04-64-3				P04-64-4		P04-64-5	
An. no.	62	63	64	65	13	14	15	16	18	19	20	21
SiO_2	0.5	0.5	0.5	0.5	0.3	0.5	0.3	0.4	0.3	0.4	0.5	0.6
CaO	1.3	1.3	1.4	1.3	1.4	1.7	1.5	1.5	1.1	1.5	1.2	1.3
P_2O_5	30.8	30.3	30.8	31.0	30.8	30.9	31.0	30.5	30.5	30.9	30.3	30.4
La_2O_3	11.6	11.8	12.0	11.8	12.9	11.6	12.8	12.4	11.7	12.9	11.0	10.6
Ce_2O_3	26.1	26.2	25.7	26.4	26.9	24.6	25.6	25.6	26.1	24.8	25.2	24.7
Pr_2O_3	2.6	2.6	2.5	2.4	2.8	2.5	2.4	2.7	2.7	2.3	2.9	2.7
Nd_2O_3	10.3	10.3	10.0	10.2	9.5	9.5	9.2	9.3	10.2	8.3	10.8	10.6
Sm_2O_3	2.3	2.1	2.3	2.3	2.2	2.4	2.1	2.3	2.4	2.2	2.4	2.3
Gd_2O_3	1.9	2.0	1.8	2.0	1.8	2.2	1.7	1.7	1.8	1.7	1.9	1.9
Y_2O_3	3.1	3.2	2.9	3.1	2.7	3.1	2.6	2.7	2.6	2.7	3.3	3.5
ThO_2	6.9	6.5	7.4	6.3	5.9	8.2	6.6	7.6	4.8	7.2	6.5	7.0
UO_2	1.0	1.0	1.1	1.1	1.2	1.6	1.3	1.3	1.4	1.3	1.4	1.3
Total	98.5	97.8	98.4	98.3	98.3	98.8	97.1	98.0	95.7	96.1	97.3	97.0
Ca/Th + U	0.8	0.8	0.8	0.9	0.9	0.8	0.9	0.8	0.8	0.8	0.7	0.7

Location of the sample P04-64: N 41° 43,947′; E 24° 41,717′.

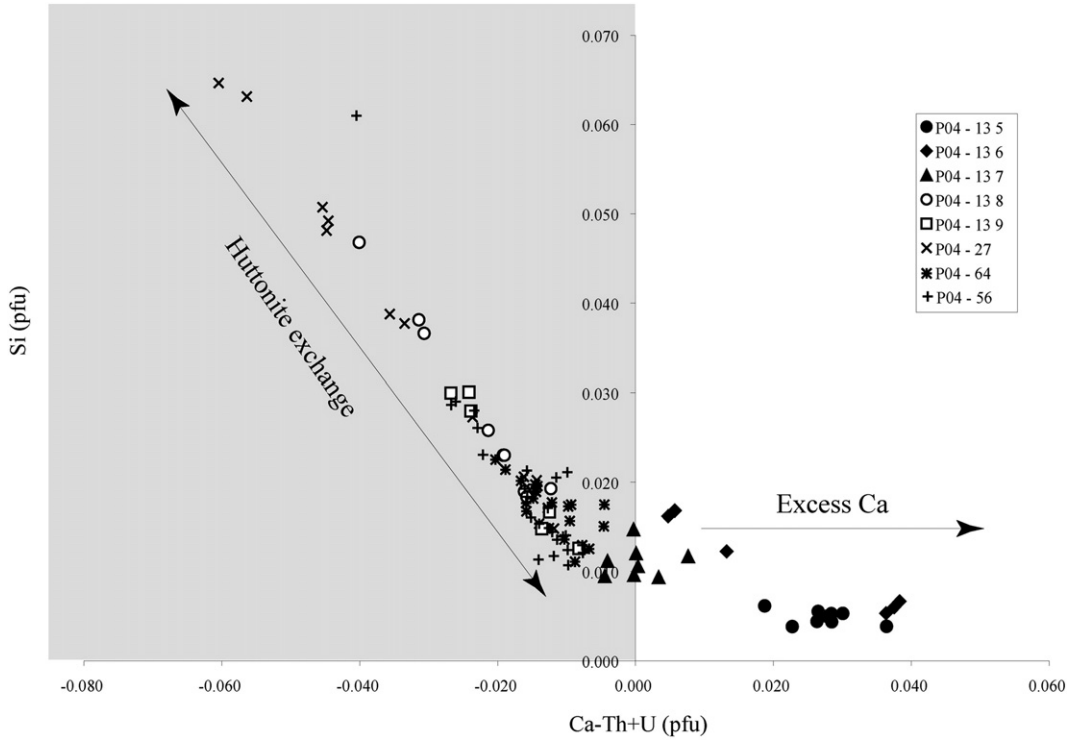

Fig. 5. Ca − (Th + U) versus Si diagram (per formula for 4 oxygens) in the investigated monazite grains. Ca − (Th + U) > 0 indicate that Ca is involved in the brabantite exchange and other substitution schemes (REE, P; Chang et al., 1998; Williams et al., 2006).

In summary, element mapping (Figs. 3 and 4) shows that, in comparison to monazites from the CSZ, those from the NSZ display strong and complex chemical zonations. These are traditionally interpreted as a consequence of episodic growth or dissolution/recrystallization of monazite in response to changing environments (Zhu and O'Nions, 1999a, Bea and Montero, 1999, Foster et al., 2000; Spear and Pyle, 2002).

5.2. Th–Pb data

In the NSZ, five monazite grains from sample P04-13 and one monazite grain from sample P04-27 have been investigated for ^{232}Th–^{208}Pb analyses based on BSE images (Table 2a and Fig. 3). In P04-13 the ages range from 38.6 ± 1.1 Ma to 54.9 ± 1.7 Ma. This age scattering corresponds to differences between individual grains (up to 16 Ma: see Fig. 3e and 3 m) as well as heterogeneities within a single grain (up to 12 Ma, Fig. 3i). In P04-13-5, P04-13-6 and P04-13-7, the oldest ages are within the cores whereas younger ages are recorded close to the rims (Fig. 3a, e and i). In contrast, P04-13-8 and P04-13-9 show no significant age scattering (Fig. 3m and q). Ages for P04-27 range from 40.3 ± 1.2 to 44.6 ± 1.2 Ma with the youngest ages lying within the rim (Fig. 3u).

In the CSZ, eight monazite grains from sample P04-64 and four monazite grains from sample P04-56 have been investigated for ^{232}Th–^{208}Pb analyses (Table 2a and Fig. 4). For P04-64, the ages range between 34.6 ± 1.4 and 37.7 ± 1.1 Ma (Fig. 4j, m, p and s). Within sample P04-56, one monazite yields an age of 42.1 ± 1.2 Ma whereas the other grains yield distinctly older ages of between 266.4 ± 8.2 and 297.3 ± 11.4 Ma (Fig. 4a, d and g; Table 2a).

Focusing on Cenozoic ages, Fig. 6 illustrates the contrast between the NSZ and the CSZ in terms of age scattering. The scattering for the NSZ is well above analytical uncertainty (± 1.7 Ma or less), and occurs within both samples and grains. In the case of the CSZ, ages differ only between samples P04-64 and P04-56, which are two samples lying at distinctly different structural levels of the metamorphic pile (see Section 3).

5.3. Chemical versus isotopic domains

Scattering of the ^{232}Th–^{208}Pb ages is a striking feature of the NSZ monazite grains, which also display large chemical heterogeneities. All grains show chemical zoning, regardless of the existence of intra-grain age domains. Where ages vary within a grain, these variations appear to coincide with chemical domains (Fig. 3). However, a simple chemical characterization of old versus young domains appears difficult. For example, grains P04-13-7 and P04-27 tend to display older ages in Th-rich and Y-poor domains (Fig. 3i, j, k, u, v and w) with distinct ThO_2 and Y_2O_3 contents (Tab 1a and b), yet the opposite relationship is observed for P04-13-6 (Fig. 3e, f and g).

In contrast, monazite crystals from sample P04-64 yield consistent ^{232}Th–^{208}Pb ages (Fig. 6), and are chemically nearly homogeneous (Table 1c). In sample P04-56, large chemical differences occur only between monazite crystals, which clearly belong to distinct generations (Permian versus Cenozoic).

6. Complementary geochronological constraints

6.1. U–Pb zircon data

Zircon grains have been investigated for U–Pb analyses based on cathodoluminescence images. Two samples from the NSZ have been studied (P04-13 and P04-26), revealing two distinct groups of age (Fig. 7):

1) One zircon from sample P04-26 yields similar ^{206}Pb–^{238}U and ^{207}Pb–^{235}U ages of 48.7 ± 2.3 Ma and 49.5 ± 4.5 in the core, and 48.2 ± 2.2 and 49.6 ± 3.9 Ma in the rim, respectively (Table 2b). Such ages corroborate those obtained on monazite in samples P04-13 and P04-27. This zircon shows a fine oscillatory zoning typical of magmatic zircon and lacks any rim overgrowth (zircon P04-26-2, Fig. 7).
2) All other analyzed zircon grains (40 analyses) yield ^{206}Pb–^{238}U ages between 121 ± 5 and 159 ± 7 Ma (Table 2c). Even if core and rim often display indistinguishable ages, some grains yield a significantly older core with respect to the rim, with a difference of up to 20 Ma. Zircon from this second group displays various zoning

Table 2a
Th–Pb results on the monazites.

Sample	Isotopic ratios		Ages (Ma)	
	$^{208}Pb/^{232}Th$	2σ (%)	$^{208}Pb/^{232}Th$	2σ
NSZ				
P04-13-5	0.0026	3.2	49.3	1.6
P04-13-5	0.0024	3.1	51.7	1.6
P04-13-6	0.0019	2.9	38.6	1.1
P04-13-6	0.0022	3.4	45.0	1.5
P04-13-7	0.0021	2.8	43.0	1.2
P04-13-7	0.0027	3.0	54.6	1.7
P04-13-7	0.0026	3.1	51.7	1.6
P04-13-7	0.0023	3.4	46.2	1.6
P04-13-8	0.0027	3.0	54.1	1.6
P04-13-8	0.0027	3.0	53.9	1.6
P04-13-8	0.0027	3.0	54.9	1.7
P04-13-9	0.0026	3.1	51.8	1.6
P04-13-9	0.0025	3.2	50.8	1.6
P04-27	0.0022	2.7	44.6	1.2
P04-27	0.0020	2.9	40.3	1.2
P04-27	0.0021	2.8	42.9	1.2
CSZ				
P04-56-1	0.0021	2.8	42.1	1.2
P04-56-2	0.0144	3.0	288.8	8.8
P04-56-2	0.0133	3.1	266.4	8.2
P04-56-3	0.0146	3.8	292.4	11.1
P04-56-3	0.0148	3.8	297.3	11.4
P04-56-4	0.0144	3.8	289.2	11.0
P04-56-4	0.0146	3.9	293.5	11.3
P04-56-4	0.0141	3.8	283.9	10.8
P04-64-1	0.0018	3.0	37.1	1.1
P04-64-1	0.0018	3.0	36.4	1.1
P04-64-2	0.0019	3.0	37.7	1.1
P04-64-2	0.0018	3.0	36.9	1.1
P04-64-3	0.0017	3.5	35.3	1.2
P04-64-3	0.0018	4.0	36.6	1.5
P04-64-4	0.0018	4.0	36.6	1.5
P04-64-4	0.0018	4.0	36.2	1.5
P04-64-4	0.0018	4.0	36.4	1.5
P04-64-5	0.0018	4.0	36.2	1.5
P04-64-5	0.0018	4.0	36.2	1.5
P04-64-6	0.0018	4.1	35.9	1.5
P04-64-6	0.0018	4.0	36.2	1.5
P04-64-7	0.0017	4.1	34.6	1.4
P04-64-7	0.0018	4.1	35.5	1.4
P04-64-8	0.0018	4.0	37.0	1.5

patterns but usually preserves cores with a coarse growth zoning and irregular overgrowth domains with uniformly high U contents (see zircons P04-13-9 and P04-13-11 in Fig. 7). Such features are characteristic of medium-to-high grade metamorphic zircon (Corfu et al., 2003).

These results support the view that Mesozoic zircon grains represent inherited xenocrysts. They further show that Cenozoic migmatization has barely been recorded by zircons across the NSZ, as also illustrated by the results of Liati (2005) in equivalent rocks further west.

In the case of the CSZ, seven zircon grains from sample P04-56 and four from sample P04-64 have been investigated. All grains from P04-56 yield ^{206}Pb–^{238}U ages of between 38.9 ± 1.3 and 44.6 ± 1.8 Ma (^{207}Pb–^{235}U ages: 39.0 ± 2.2 and 46.9 ± 2.6 Ma) (Table 2d and Fig. 7). The maximum intra-grain age difference is 4.3 Ma. These ages corroborate the age of 42.1 ± 1.2 Ma obtained for one monazite grain in P04-56. Zircon shows oscillatory zoning resembling that seen in magmatic zircon (Fig. 7, Corfu et al., 2003). The four zircon grains from sample P04-64 yield ^{206}Pb–^{238}U ages of between 77.3 ± 2.4 and 235.2 ± 7.7 Ma (^{207}Pb–^{235}U ages: 79.5 ± 4.3 and 237.6 ± 12.9 Ma, Table 2d). These grains show inherited cores surrounded by markedly irregular and complex overgrowth domains (Fig. 7). The core versus rim age difference reaches 146 Ma in grain P04-64-2 (Table 2c). Even the youngest age, at ~77 Ma, is significantly older than the age of ca. 36 Ma consistently obtained for the monazites of the same sample (Figs. 6 and 7).

6.2. ^{39}Ar–^{40}Ar data

Muscovite from sample P04-64 (CSZ) displays a very flat age spectrum (Fig. 8) with a plateau age of 34.9 ± 0.1 Ma (1σ level; 98.8% of $^{39}Ar_K$ released). Biotite from sample P04-27 (NSZ) yields a plateau age of 34.3 ± 0.2 Ma (1σ level; 80% of $^{39}Ar_K$ released; Fig. 8). Muscovite from sample P04-13 (NSZ) yields a "plateau" age of 33.2 ± 0.3 Ma (1σ level; 96% of $^{39}Ar_K$ released), slightly younger than the age of biotite P04-27. On closer inspection, this experiment shows a subtle, but characteristic, saddle-shaped age spectrum (Fig. 8). Such age spectra for single grains of muscovite have been interpreted as reflecting the mixing of two isotopic domains: an inherited or initial domain, and a recrystallized or neocrystallized sub-domain (e.g., Cheilletz et al., 1999, Alexandrov et al., 2002). According to this view, the initial crystallization for muscovite P04-13 would have occurred at, or slightly before, ~34 Ma whereas the disruption event, which could be linked to deformation-induced and/or fluid-induced recrystallization, would have occurred at ~32 Ma, or slightly later. In this scenario, the younger re- or neo-crystallized domain may either characterize a disruption event, unconnected to the initial crystallization of the muscovite, or the last isotopic record during a protracted (re)crystallization history.

7. Oxygen isotopes

Qtz and Fd have variable $\delta^{18}O$ values, in the range of 10.1–21.7‰ and 7.6–12.7‰, respectively (Table 3). Samples from the CSZ (P04-56 and P04-64) have Qtz–Fd oxygen isotope fractionation ($\Delta^{18}O_{Qtz-Fd}$) of 2.5 and 2.8‰ (Fig. 9), consistent with equilibration at metamorphic temperatures. For instance, if the feldspar is taken to consist of equal proportions of K-feldspar + Albite + Anorthite, the temperature of equilibration would be ~350–400 °C using the fractionation factors of

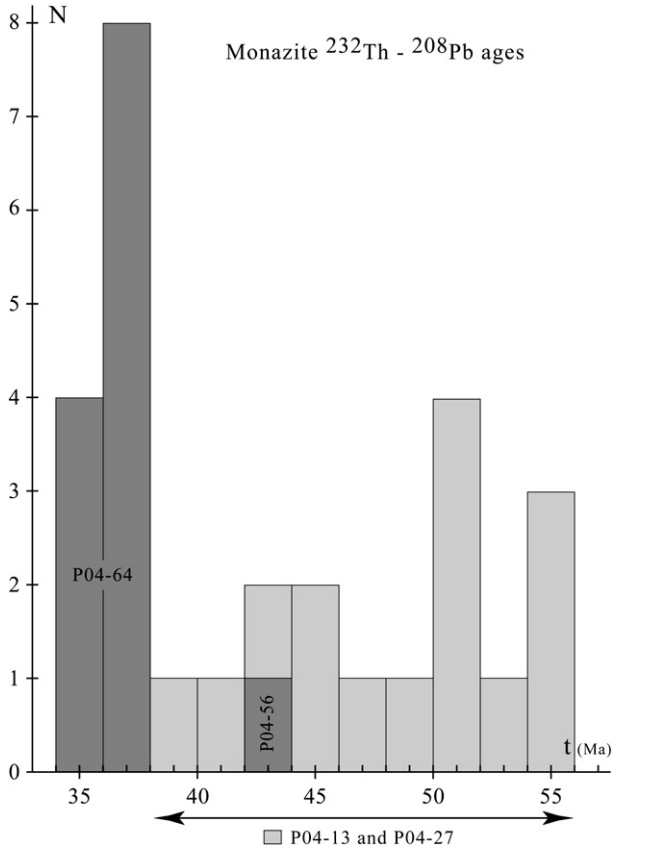

Fig. 6. Histogram of Cenozoic monazite ^{232}Th–^{208}Pb ages. The bar width corresponds approximately to the age error bar (2σ level).

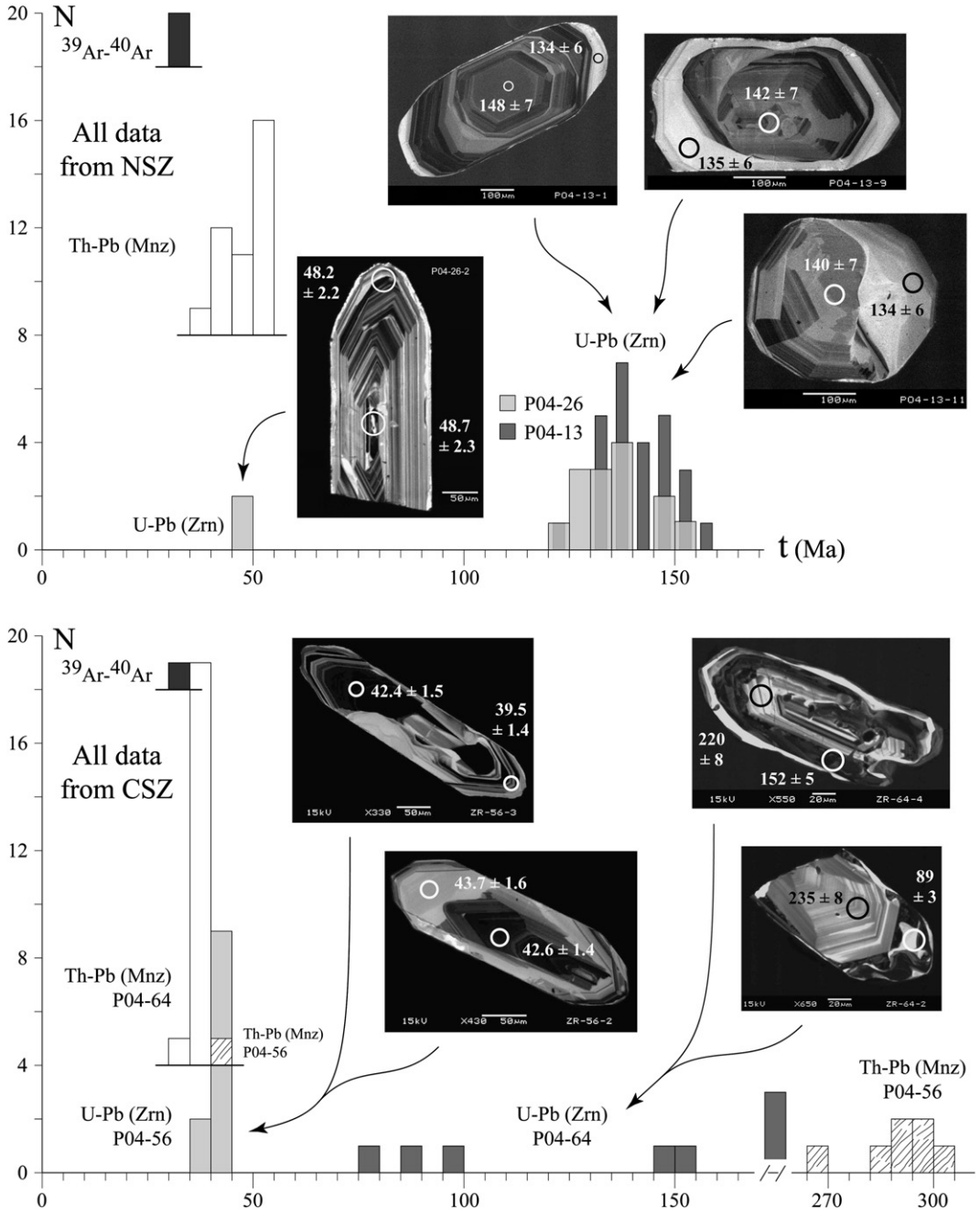

Fig. 7. Histograms of the complete geochronological dataset obtained in this study. Cathodoluminescence images of representative zircon grains show measured ^{206}Pb–^{238}U ages (2σ level). See the text for explanation.

Zheng (1993). Minerals of sample P04-56 have the lowest $\delta^{18}O$ values (Fig. 9). This vein is hosted by amphibolites, which is the metamorphic equivalent of a relatively low $\delta^{18}O$ basic rock (e.g., Matthews et al., 1996). In contrast, P04-64 is hosted by gneisses, and its minerals have the usual values for pegmatites (e.g., Matthews et al., 2003). Hence, it seems that the nature of the immediate host rock has played a role in buffering the $\delta^{18}O$ value of the veins. Qualitatively, this indicates relatively low fluid–rock ratios during the interaction.

In samples from the NSZ (P04-13 and 27), quartz has a much higher $\delta^{18}O$ value than the coexisting feldspar, with $\Delta^{18}O_{Qtz-Fd}$ reaching 4 to 9% (Table 3). While feldspars display common values for pegmatites, quartz exhibits unusually high values ($\delta^{18}O$ up to 21.7‰). The origin of this unusual signature is discussed further below.

Table 2b
U–Pb results on the P04-26 magmatic zircon (C: core and R: rim).

Sample	Isotopic ratios				Rho	Ages (Ma)			
	$^{206}Pb/^{238}U$	2σ%	$^{207}Pb/^{235}U$	2σ%		$^{206}Pb/^{238}U$	2σ	$^{207}Pb/^{235}U$	2σ
P04-26-2 C	0.008	4.8	0.050	9.1	0.52	48.7	2.3	49.5	4.5
P04-26-2 R	0.008	4.6	0.050	7.9	0.58	48.2	2.2	49.6	3.9

8. Discussion

8.1. Monazite zoning and age scattering

Permian and Mesozoic ages have been obtained for monazite and zircon grains from the CSZ, while mid-Mesozoic ages have been obtained for most of the zircon grains from the NSZ (Fig. 7). These ages

Table 2c
U–Pb results on the P04-13 and P04-26 metamorphic zircons (C: core and R: rim).

Sample	Isotopic ratios				Rho	Ages (Ma)			
	$^{206}Pb/^{238}U$	2σ%	$^{207}Pb/^{235}U$	2σ%		$^{206}Pb/^{238}U$	2σ	$^{207}Pb/^{235}U$	2σ
P04-26-1 C	0.022	4.6	0.153	6.7	0.7	138.9	6.4	144.8	9.6
P04-26-1 R	0.023	4.5	0.149	6.6	0.7	145.1	6.6	140.8	9.3
P04-26-3 C	0.022	4.6	0.149	7.0	0.7	139.0	6.4	141.1	9.9
P04-26-3 R	0.020	4.6	0.149	7.0	0.7	125.5	5.8	132.8	9.1
P04-26-4 C	0.024	4.6	0.165	6.7	0.7	153.5	7.1	154.7	10.3
P04-26-4 R	0.021	4.5	0.137	6.5	0.7	132.7	6.0	130.3	8.5
P04-26-9 C	0.023	4.5	0.159	6.6	0.7	148.3	6.7	150.0	9.8
P04-26-9 R	0.020	4.6	0.134	6.8	0.7	127.7	5.8	127.7	8.7
P04-26-5 C	0.021	4.7	0.153	7.5	0.6	136.1	6.4	144.2	10.8
P04-26-6 C	0.019	4.7	0.119	8.2	0.6	121.1	5.7	114.1	9.4
P04-26-7 C	0.020	4.7	0.133	8.0	0.6	127.8	6.0	127.0	10.2
P04-26-8 C	0.021	4.6	0.141	7.0	0.7	133.2	6.1	133.8	9.4
P04-26-10 C	0.021	5.3	0.145	7.4	0.7	136.1	7.2	137.5	10.2
P04-26-10 R	0.021	5.2	0.144	8.2	0.6	134.9	7.0	136.9	11.2
P04-13-1 C	0.023	4.5	0.159	6.5	0.7	148.3	6.7	150.0	9.8
P04-13-1 R	0.021	4.6	0.142	6.6	0.7	134.2	6.1	134.9	8.8
P04-13-2 C	0.022	4.6	0.150	6.6	0.7	142.1	6.5	141.5	9.3
P04-13-2 R	0.019	4.6	0.129	6.6	0.7	120.6	5.5	122.8	8.1
P04-13-3 C	0.022	4.7	0.146	7.1	0.7	137.4	6.4	138.5	9.8
P04-13-4 C	0.022	4.6	0.157	6.7	0.7	137.6	6.3	148.1	9.9
P04-13-4 R	0.021	4.6	0.165	6.7	0.7	136.3	6.2	154.8	10.4
P04-13-5 C	0.021	4.5	0.141	6.6	0.7	132.6	6.0	133.6	8.8
P04-13-5 R	0.021	4.5	0.140	6.5	0.7	132.6	6.0	133.3	8.6
P04-13-6 C	0.023	4.6	0.153	6.6	0.7	145.7	6.7	144.2	9.5
P04-13-6 R1	0.024	4.5	0.162	6.5	0.7	152.3	6.9	152.3	9.9
P04-13-6 R2	0.021	4.6	0.142	6.5	0.7	135.7	6.2	135.0	8.8
P04-13-7 C	0.021	4.6	0.144	6.7	0.7	136.9	6.3	136.6	9.2
P04-13-8 C	0.023	4.6	0.155	6.6	0.7	145.3	6.7	146.7	9.6
P04-13-8 R	0.025	4.5	0.162	6.5	0.7	158.8	7.2	152.8	9.9
P04-13-9 C	0.022	4.6	0.150	6.9	0.7	142.2	6.6	142.2	9.8
P04-13-9 R	0.021	4.7	0.143	7.9	0.6	134.5	6.3	135.5	10.7
P04-13-10 C	0.023	4.6	0.152	6.6	0.7	144.2	6.7	143.8	9.5
P04-13-10 R	0.024	4.6	0.167	6.8	0.7	154.1	7.2	157.2	10.6
P04-13-11 C	0.022	4.7	0.156	6.8	0.7	139.9	6.5	147.0	10.0
P04-13-11 R	0.021	4.6	0.141	6.9	0.7	133.6	6.2	134.2	9.2
P04-13-12 R	0.022	4.6	0.144	6.9	0.7	137.1	6.3	136.4	9.4
P04-13-2a C	0.023	5.0	0.153	7.3	0.7	146.2	7.3	144.2	10.6
P04-13-3a C	0.024	5.0	0.164	7.5	0.7	152.2	7.5	154.3	11.5
P04-13-4a C	0.022	5.0	0.151	7.4	0.7	140.5	7.0	142.7	10.5
P04-13-4a R	0.023	5.0	0.153	6.7	0.7	149.3	7.4	144.5	9.7

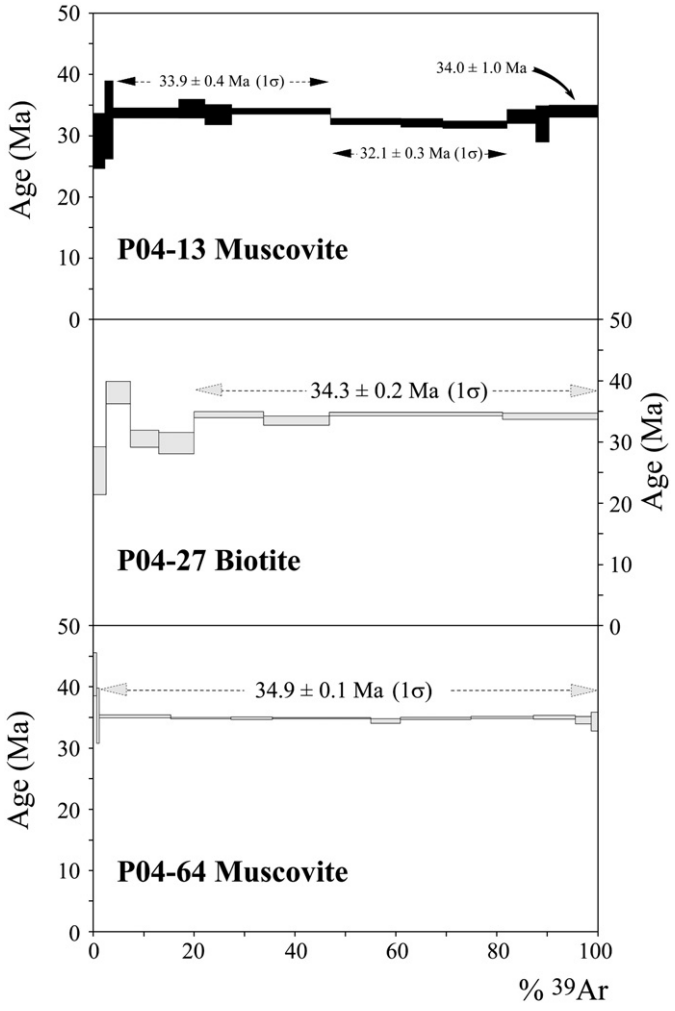

Fig. 8. Single-grain ^{39}Ar–^{40}Ar age spectra. Age error bars for each temperature step are at the 1σ level and do not include errors in the *J*-values. The errors in the *J*-values are included in the plateau age calculations.

are reminiscent of the first and second age groups described in Section 2.2. The actual timing of the emplacement of the veins is blurred by inheritance from distinct protoliths. Cenozoic U–Th–Pb ages have been obtained in one zircon from sample P04-26, and in all monazite grains, except those inherited from a Permian protolith in sample P04-56. Muscovite and biotite ^{39}Ar–^{40}Ar ages closely follow the Cenozoic U–Th–Pb ages (Fig. 7). These Cenozoic ages correlate well with the third group of ages previously obtained in both shear zones.

Table 2d
U–Pb results on the P04-56 and the P04-64 zircons (C: core and R: rim).

Sample	Isotopic ratios				Rho	Ages (Ma)			
	$^{206}Pb/^{238}U$	2σ%	$^{207}Pb/^{235}U$	2σ%		$^{206}Pb/^{238}U$	2σ	$^{207}Pb/^{235}U$	2σ
P04-56-1 C	0.007	4.4	0.042	14.4	0.3	42.6	1.9	42.0	6.1
P04-56-1 R	0.007	4.0	0.046	11.5	0.3	44.6	1.8	45.7	5.3
P04-56-2 C	0.007	3.2	0.043	5.8	0.6	42.6	1.4	43.2	2.5
P04-56-2 R	0.007	3.6	0.045	9.8	0.4	43.7	1.6	44.7	4.4
P04-56-3 C	0.007	3.4	0.042	6.9	0.5	42.4	1.5	42.1	2.9
P04-56-3 R	0.006	3.6	0.044	7.2	0.5	39.5	1.4	43.9	3.1
P04-56-5 R	0.007	3.4	0.043	6.2	0.6	42.5	1.5	43.2	2.7
P04-56-6 R	0.007	3.4	0.047	5.6	0.6	44.3	1.5	46.9	2.6
P04-56-7 C	0.007	3.4	0.045	5.7	0.6	43.0	1.5	44.8	2.5
P04-56-8 R	0.006	3.4	0.039	5.6	0.6	38.9	1.3	39.0	2.2
P04-56-8 C	0.007	3.6	0.045	6.4	0.6	43.2	1.6	44.2	2.8
P04-64-1 R	0.012	3.2	0.081	5.4	0.6	77.3	2.4	79.5	4.3
P04-64-1 C	0.023	3.3	0.155	5.2	0.6	148.9	4.8	145.9	7.5
P04-64-2 C	0.037	3.3	0.264	5.4	0.6	235.2	7.7	237.6	12.9
P04-64-2 R	0.014	3.6	0.095	6.4	0.6	89.2	3.2	91.9	5.9
P04-64-3 C	0.034	3.3	0.240	5.1	0.6	213.5	6.9	218.4	11.1
P04-64-3 R	0.015	3.4	0.103	5.3	0.6	97.4	3.3	99.3	5.3
P04-64-4 C	0.035	3.4	0.246	5.6	0.6	220.0	7.6	223.3	12.5
P04-64-4 R	0.024	3.4	0.151	5.2	0.6	152.3	5.2	142.8	7.5

Beyond this broad agreement, Cenozoic monazite from the NSZ displays a significant scattering of ages (Fig. 6), and shows distinct compositions and strong chemical zonations that are spatially related to distinct age domains (Fig. 3 see Section 4.3). Nevertheless, this spatial relationship can hardly be described in terms of a consistent chemical evolution of monazite through time. This is in agreement with numerous studies describing complex zoning and patchworks of age domains related to discontinuous growth or successive dissolution/recrystallization events in monazite (Parrish, 1990; Hawkins and Bowring, 1997; Zhu and O'Nions, 1999a,b; Crowley and Ghent, 1999; Foster et al., 2002; Pyle and Spear, 2003; Kohn et al., 2005; McFarlane et al., 2006; Hinchey et al., 2007; Rasmussen and Muhling, 2007). In NSZ monazite crystals, the patchy, yet nearly concentric distribution of age domains and of Th, Y and Ca (Fig. 3) argue in favour of episodic

Table 3
Oxygen isotope composition of quartz and felspars from the pegmatitic veins.

Samples	$\delta^{18}O$ (Qtz)	$\delta^{18}O$ (Fd)	$\Delta^{18}O$(Qtz–Fd)
P 04-13	21.7	12.7	9.0
P 04-27	14.5	10.5	4.0
P 04-56	10.1	7.6	2.5
P 04-64	13.2	10.4	2.8

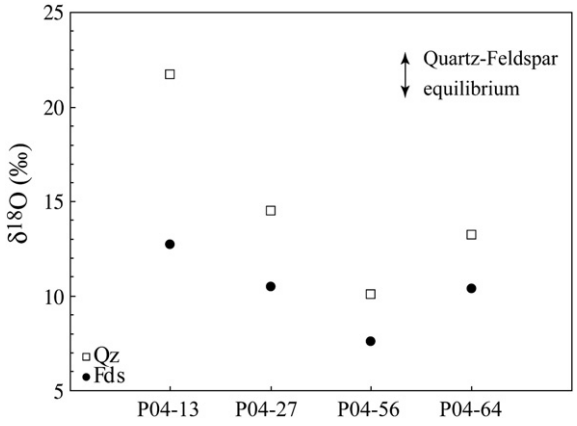

Fig. 9. Oxygen isotope composition of quartz–feldspar pairs from the four samples selected for Th–Pb monazite dating. The graph highlights isotopic equilibrium in samples from the CSZ (P04-56 and P04-64) versus disequilibrium in samples from the NSZ (P04-13 and P04-27).

growth of the monazite or the partial replacement of primary grains. In contrast, Cenozoic monazite from the CSZ yields consistent ages (Fig. 6) together with very limited chemical variations (Table 1c); this indicates that only the NSZ samples display disturbances of the U–Th–Pb systematics.

Pb diffusion is known to be slow in monazite (Smith and Giletti, 1997; Cherniak et al., 2004, Gardés et al., 2006). In contrast, experimental studies and the analysis of some natural examples have shown that dissolution/recrystallization under hydrothermal conditions is an efficient mechanism for (1) disrupting the monazite U–Th–Pb isotope systems even at low temperature conditions, and (2) producing strong chemical variations on the grain scale (Poitrasson et al., 1996; Teufel and Heinrich, 1997; Hawkins and Bowring, 1997; Poitrasson et al., 2000; Seydoux-Guillaume et al., 2002). On account of these studies and because the NSZ samples yield clear evidence of fluid–rock interactions, we suggest that fluids have played a major role in disrupting the monazite chronometer. In the following sections, we will first specify the role of fluids in the evolution of the studied pegmatites, and then discuss its impact on the chemical and isotopic signature of monazite.

8.2. Fluid–rock interactions

The studied pegmatites from the NSZ show evidence of interaction with externally derived fluids after primary crystallization. The most striking evidence is the strong quartz–feldspar isotopic disequilibrium in samples P04-13 and 27 (Fig. 9; see Section 7). In common granitic bodies and associated rocks like pegmatites, quartz is enriched in ^{18}O relative to feldspars by about 1 to 3‰, depending on feldspar composition and actual equilibrium temperature (Taylor et al., 1979). The CSZ samples display this relationship. In contrast, the NSZ samples show disequilibrium, which can only be achieved through differential exchange of minerals with an external reservoir, fluid being here the most likely candidate. The very high value reached by quartz in sample P04-13 ($\delta^{18}O = 21.7‰$) is also a clear indication that this crustal metamorphic rock has undergone isotopic re-equilibration with an external reservoir. In contrast, feldspars from the NSZ samples show typical values for pegmatites. Hence, it seems that the large Qtz–Fd difference is due to a major increase in the quartz $\delta^{18}O$ value (up to 21.7‰, compared with usual values of about 11 to 15‰ for this type of rock, e.g., Matthews et al., 2003) rather than to a retrograde alteration of feldspar. Usually, because of the lower diffusivity of ^{18}O in the quartz structure, quartz is much more resistant than feldspar to isotopic exchange with fluids. Therefore, a process capable of selectively increasing the $\delta^{18}O$ value of quartz has to be found for the present case. As described in Section 3, pegmatites P04-13 and P04-27 are characterized by a strong contrast in grain size and microstructures between quartz and feldspar. Quartz has undergone extensive dynamic recrystallization, resulting in a pronounced reduction in grain size, whereas feldspars have remained essentially intact (Fig. 2e). Associated microstructures document a deformation event that occurred at greenschist facies conditions (see Section 3). If fluids circulated through the pegmatites during this event, then the contrast in behaviour between quartz and feldspar makes it likely that quartz re-equilibrated with fluids more readily. Syn-deformation fluid circulation is documented by the precipitation of newly formed minerals in microscale tension gashes within feldspar clasts (Fig. 2f).

The isotopic record of NSZ pegmatites shows that the circulating fluid was able to impose an unusually high $\delta^{18}O$ signature on these rocks. The thick marbles in the footwall of the NSZ (see Section 2.1) constitute the most likely candidate for the initial reservoir. This view is consistent with the report of marbles with $\delta^{18}O$ values up to 28‰ in the Central Rhodope, interpreted as preserving isotopic compositions inherited from marine precursors (Matthews et al., 1996). Fluids liberated from such rocks through dehydration–decarbonation reactions would have carried the necessary $\delta^{18}O$ signature. The same isotopic signature would be obtained if fluids emanating from another source had undergone exchange with the marbles, for example as a result of infiltration along discontinuities. Such fluids should also contain calcium and consequently be capable of introducing this element into the rocks they are infiltrating. Evidence for this occurs in the pegmatites in the form of calcite precipitated within the microscale tension gashes. CO_2 itself must have been added to the pegmatites, as a constituent of a H_2O–CO_2 fluid. Since the microscale tension gashes within feldspar clasts are a component of the greenschist facies fabric, we conclude that the studied NSZ pegmatites were infiltrated by H_2O–CO_2 fluids during greenschist facies deformation.

At first sight, this conclusion is at odds with the results of Matthews et al. (1996) who showed that rocks from broadly the same area preserved their pre-metamorphic isotopic signatures and, therefore, escaped significant fluid infiltration. However, with respect to our sampling sites, the study of Matthews et al. (1996) focused on outcrops located at higher levels of the metamorphic pile, away from the part of the NSZ displaying localized greenschist facies deformation. Thus, we find no contradiction between this earlier study and ours. In fact comparison between the two supports the hypothesis that the thick marbles in the footwall of the NSZ constitute the source of the fluids that are documented here.

8.3. Chemical and isotopic disturbance of monazite

Most chemical variations observed in the NSZ monazites could be explained by the brabantite and huttonite exchanges (Fig. 5), which have been attributed to hydrothermal alteration processes (Poitrasson et al., 1996, 2000). Intra-grain variations of the Th content in distinct age and chemical domains (Fig. 3) are a good indication of interaction with fluids. As Th solubility and mobility are low during interaction between hydrothermal fluids and rocks (Rogers and Adams, 1969; Poitrasson et al., 1996), Th released during monazite dissolution processes is likely to be incorporated into newly formed overgrowths, giving rise to Th-rich and Pb-free (young) zones (Poitrasson et al., 1996, 2000; Seydoux-Guillaume et al., 2002). Since Y and HREE are more soluble than Th, their behaviour is expected to be inversely correlated with respect to Th. Th-rich overgrowths are found to be a common feature in natural monazites that have experienced fluid interactions (Hawkins and Bowring, 1997; Townsend et al., 2000). However, in some natural hydrothermal monazites from sericitized samples, Poitrasson et al. (2000) have observed strong removal of Th leading to the overgrowth of Th poor domains. These authors concluded that, under specific fluid–rock conditions, the mobility of Th might be enhanced, so that Th could be transported and

reprecipitated as a Th-rich phase or as Th-rich overgrowths on adjacent monazite grains. This variable behaviour of Th during fluid–rock interactions may explain its heterogeneous distribution as well as its variable relations with Y in the NSZ monazites (see Section 5.1). In most grains, Th increase inversely correlates with Y decrease from core to rim alongside the occurrence of younger ages (Fig. 3, see Section 5.3); in contrast, P04-13-6 shows the opposite chemical versus age relation (Fig. 3e, f and g).

Some monazite grains in P04-13 have a high Ca content, which does not seem compatible with the brabantite exchange (Fig. 5). This sample shows clear evidence of interaction with H_2O–CO_2 fluids derived from carbonates (see Section 8.2). We therefore suggest that the elevated Ca/Th + U ratio observed in monazite crystals P04-13-5, P04-13-6 and P04-13-7 also results from this fluid–rock interaction. Experiments have shown that Ca-rich fluids can enhance monazite dissolution and result in the recrystallization of grains with strong chemical modifications (Seydoux-Guillaume et al., 2002). These experiments also indicate that $CaCl_2$ fluids are more efficient in resetting the U–Th–Pb isotope system of monazite than other fluid compositions (e.g. $SrCl_2$ fluids). Hence, in the case of the NSZ, it is not surprising that fluid interactions were able to induce a significant scattering of the monazite Th–Pb ages.

8.4. Significance of the U–Th–Pb ages and concluding remarks about the monazite chronometer

In the case of the CSZ (sample P04-64), the obtained Th–Pb ages show no scattering and monazite appears to be chemically undisturbed. Oxygen isotopes show no evidence for a pervasive late-stage fluid infiltration, which is consistent with microstructures indicating that deformation has ceased at high-grade conditions. Therefore we interpret the monazite Th–Pb weighted mean age of 36.3 ± 0.4 Ma (based on 16 ages) as the age of the emplacement of this pegmatite vein. In contrast, zircon U–Pb ages from the same sample reflect inheritance from one or several Mesozoic metamorphic cycle(s) but do not display any record of the Cenozoic event. Sample P04-56, at a higher level in the metamorphic pile (above the CSZ), has yielded one monazite Th–Pb age of 42.1 ± 1.2 Ma and a zircon ^{206}Pb–^{238}U weighted mean age of 42.1 ± 1.3 Ma (11 spots), both ages are interpreted as dating the emplacement of this vein. In this sample, Paleozoic ages are preserved in several monazites, but not in zircon. This contrasting behaviour of the two chronometers (Th–Pb in monazite versus U–Pb in zircon) between samples P04-56 and P04-64 could be explained by distinct protoliths from which the pegmatites derive. As pointed out in Section 3, P04-56 is hosted by amphibolites whereas the dominant host rocks of P04-64 are felsic gneisses. In the case of P04-56, field relations do not demonstrably document that the vein emanates from the host amphibolites, but a strong influence from the wall rocks is nevertheless recorded by the low $\delta^{18}O$ signature of the sample (see Section 7). In amphibolites, zirconium is mainly stored in amphibole (or garnet and biotite) and can be released to produce zircon if breakdown of these phases occurs, for instance during partial melting of the amphibolites (Hoskin and Schaltegger, 2003). Monazite is generally rare in rocks with mafic–calcic compositions such as amphibolites and pegmatites (Spear and Pyle, 2002). In the absence of fluids, the few existing grains can preserve old ages even at high temperature because the diffusion rate of Pb is very low (Smith and Giletti, 1997; Cherniak et al., 2004; Seydoux-Guillaume et al., 2002; Gardés et al., 2006). In contrast, felsic gneisses usually contain abundant pre-existing zircon and their recrystallization can produce overgrowth domains that surround inherited cores (Hoskin and Schaltegger, 2003). In the case of polycyclic metamorphic evolution, this may result in complex textures in the zircon grains that are not easy to decipher, such as in sample P04-64 (Fig. 7). Pre-existing monazite was not found in sample P04-64. This suggests that if monazite was previously present, it was entirely dissolved into the melt during Cenozoic partial melting. Newly-formed monazite may either precipitate as a result of partial melting or of melt crystallization (Williams et al., 2006). In both cases, the monazite Th–Pb chronometer records the formation age of the P04-64 pegmatite.

In the case of the NSZ, where pronounced fluid interactions occurred during greenschist facies deformation, scattered monazite ages are more difficult to interpret. Nevertheless, the oldest monazite Th–Pb ages span the ^{206}Pb–^{238}U age of 48–49 ± 2 Ma obtained on a magmatic zircon from sample P04-26. Field relations show that all the veins studied were formed and emplaced at high-grade conditions, which strongly suggests that they are subcontemporaneous. Noticeably, no veins at this level of the metamorphic pile display relations suggesting a late emplacement in a cooled environment. Hence, the Th–Pb ages of ~49 to 55 Ma, and especially those obtained in seemingly undisturbed monazite grains (P04-13-8 and P04-13-9, at 50.8 ± 1.8 to 54.9 ± 1.7 Ma) probably relate to the emplacement of the studied pegmatites. The spread of younger Th–Pb ages (from 38.6 ± 1.1 to 46.2 ± 1.6 Ma) may reflect the timing of fluid circulations during progressive cooling to greenschist facies conditions or it may reflect variable perturbations of the monazite isotope system during the fluid-assisted greenschist facies deformation stage, the age of which, therefore, would be ≤39 Ma. This is consistent with ^{39}Ar–^{40}Ar mica ages of ~32 to 34 Ma, which can be taken as a tighter constraint for the timing of the greenschist facies stage.

The above results illustrate the capacity of monazite to record distinct events in a single rock. They also indicate that this record may vary significantly from one grain to another. The contrasting behaviours of the Th–Pb monazite and U–Pb zircon chronometers between different samples also support the view that temperature is not the main parameter controlling the resetting of isotope systems. In addition, the nature of the protoliths, as well as the presence (or absence) of fluids enhancing dissolution/recrystallization processes, appears to play a major role. Due to its wide occurrence in geological systems, monazite is a powerful chronometer. However, as illustrated by this study, a careful inspection of the possible involvement of fluids is needed in order for a meaningful interpretation of the ages to be proposed. For this reason, and for a better understanding of the U–Th–Pb data in general, information provided by complementary methods such as element mapping, oxygen isotopes, petro-microstructural observations, and the record of other chronometers appears essential.

Acknowledgments

Field work was funded by NATO (Collaborative Linkage Grant No. 978915).

Thanks are due to Mireille Besairie in Clermont Ferrand for her help in mineral separation, to the three anonymous reviewers and the Guest Editor Axel Guerdes for their reviews that significantly improve the manuscript, and to Jean Yves Bosse-Vidal and Fran van Wyk de Vries for English corrections.

Appendix A. Supplementary data

Supplementary data associated with this article can be found in the online version, at doi:10.1016/j.chemgeo.2008.10.025.

References

Alexandrov, P., Ruffet, G., Cheilletz, A., 2002. Muscovite recrystallization and saddle-shaped $^{40}Ar/^{39}Ar$ age spectra: examples from the Blond granite (Massif Central, France). Geochimica et Cosmochimica Acta 66, 1793–1807.

Arkadakskiy, S., Böhm, C., Heaman, L., Cherneva, Z., Stancheva, E., 2000. New U–Pb age results from the Central Rhodope Mts., Bulgaria. ABCD-GEODE Workshop, Borovets, Bulgaria, p. 5.

Barr, S.R., Temperley, S., Tarney, J., 1999. Lateral growth of the continental crust through deep level subduction–accretion: a re-evaluation of central Greek Rhodope. Lithos 46, 69–94.

Bea, F., Montero, P., 1999. Behavior of accessory phases and redistribution of Zr, REE, Y, Th and U during metamorphism and partial melting of metapelites in the lower crust: an example from the Kinzigite Formation of Ivrea-Verbano, NW Italy. Geochimica et Cosmochimica Acta 63, 1133–1153.

Bonev, N., Burg, J.P., Ivanov, Z., 2006. Mesozoic-Tertiary structural evolution of an extensional gneiss dome: the Kesebir–Kardamos dome, eastern Rhodope (Bulgaria-Greece). International Journal of Earth Sciences 95, 318–340.

Bosse, V., Gautier, P., Tiepolo, M., Paquette, J.L., Cherneva, Z., Richard, L., 2006. Evolution des roches polymétamorphiques à reliques UHP du Rhodope (Grèce, Bulgarie): l'apport de la datation in situ U–Th–Pb par ICP-MS ablation laser. Proceedings Réun. Sci. Terre, Dijon, France, p. 46.

Burg, J.P., Ivanov, Z., Ricou, L.E., Dimov, D., Klain, L., 1990. Implications of shear-sense criteria for the tectonic evolution of the Central Rhodope massif, southern Bulgaria. Geology 18, 451–454.

Catlos, E.J., Gilley, L.D., Harrison, T.M., 2002. Interpretation of monazite ages obtained via in situ analysis. Chemical Geology 188, 193–215.

Chang, L.L.Y., Howie, R.A., Zussman, J., 1998. Rock-forming minerals. Non-Silicates: Sulphates, Carbonates, Phosphates and Halides, vol. 5B. Longman Group, Harlow, UK.

Cheilletz, A., Ruffet, G., Marignac, C., Kolli, O., Gasquet, D., Féraud, G., Bouillin, J.P., 1999. $^{40}Ar/^{39}Ar$ dating of shear zones in the Variscan basement of the Greater Kabylia (Algeria). Evidence of an Eo-Alpine event at 128 Ma (Hauterivian–Barremian boundary): geodynamic consequences. Tectonophysics 306, 97–116.

Cherneva, Z., Georgieva, M., 2005. Metamorphozed Hercynian granitoids in the Alpine structures of the Central Rhodope, Bulgaria: geotectonic position and geochemistry. Lithos 82, 149–168.

Cherniak, D.J., Watson, B.E., Grove, M., Harrison, T.M., 2004. Pb diffusion in monazite: a combined RBS/SIMS study. Geochimica and Cosmochimica Acta 68, 829–840.

Clayton, R.N., Mayeda, T.K., 1963. The use of bromine pentafluoride in the extraction of oxygen from oxides and silicates for isotopic analysis. Geochimica et Cosmochimica Acta 27, 43–52.

Corfu, F., Hanchar, J., Hoskin, P.W.O., Kinny, P., 2003. Atlas of zircon textures. In: Hanchar, J.M., Hoskin, P.W.O. (Eds.), Ziron, Reviews in Mineralogy and Geochemistry, vol. 53. Mineralogical Society of America, pp. 468–500.

Crowley, J.L., Ghent, E.D., 1999. An electron microprobe study of the U–Th–Pb systematics of metamorphosed monazite: the role of Pb diffusion versus overgrowth and recrystallization. Chemical Geology 157, 285–302.

Cruz, M.J., Cunha, J.C., Merlet, C., Sabaté, P., 1996. Dataçao pontual das monazitas da regiao de Itambe, Bahia, através da microssonda electrônica. XXXIX Congresso Brasileiro de Geologia, pp. 206–209.

Dimov, D., Cherneva, Z., Georgiev, J., Arkadakskiy, S., 1996. Structural position of the migmatic formations and metabasites within the ductile shear zone in the Chepelarska River Valley, north of Chepelare. Review of the Bulgarian Geological Society 57 (1), 47–52.

Dinter, D.A., 1998. Late Cenozoic extension of the Alpine collisional orogen, northeastern Greece: origin of the north Aegean basin. Geological Society of America bulletin 110, 1208–1230.

Di Vincenzo, G., Carosi, R., Palmeri, R., Tiepolo, M., 2007. A comparative U–Th–Pb (zircon–monazite) and 39Ar–40Ar (muscovite–biotite) study of shear zones in northern Victoria Land (Antarctica): implications for geochronology and localized reworking of the Ross Orogen. Journal of Metamorphic Geology 25, 605–630.

Foster, G., Kinny, P., Vance, D., Prince, C., Harris, N., 2000. The significance of monazite U–Th–Pb age data in metamorphic assemblages; a combined study of monazite and garnet chronometry. Earth and Planetary Sciences 181, 327–340.

Foster, G., Gibson, H.D., Parrish, R., Horstwood, M., Fraser, J., Tindle, J., 2002. Textural, chemical and isotopic insights into the nature and behaviour of metamorphic monazite. Chemical Geology 191, 183–207.

Gapais, D., 1989. Shear structures within deformed granites: mechanical and thermal indicators. Geology 17, 1144–1147.

Gardés, E., Jaoul, O., Montel, J.M., Seydoux-Guillaume, A.M., Wirth, R., 2006. Pb diffusion in monazite: an experimental study of $Pb^{2+} + Th^{4+} \leftrightarrow 2Nd^{3+}$ interdiffusion. Geochimica and Cosmochimica Acta 70, 2325–2336.

Gerdjikov, I., Gautier, P., Cherneva, Z., Kostopoulos, D., 2003. Tectonic setting of ultrahigh-pressure metamorphic rocks form the Chepelare area, Central Rhodope. Proceedings Bulgarian Geol. Soc. Annual Conf., Sofia, pp. 44–45.

Goncalves, P., Williams, M.L., Jercinovic, M.J., 2005. Electron-microprobe age mapping of monazite. American Mineralogist 90, 578–585.

Hawkins, D., Bowring, S., 1997. U–Pb systematics of monazite and xenotime: case studies from the Paleoproterozoïc of the Grand Canyon, Arizona. Contribution to Mineralogy and Petrology 127, 87–103.

Hinchey, A.M., Carr, S.D., Rayner, N., 2007. Bulk compositional controls on the preservation of age domains within metamorphic monazite: a case study from quartzite and garnet–cordierite–gedrite gneiss of Thor-Odin dome, Monashee complex, Canadian Cordillera. Chemical Geology 240, 85–102.

Hoskin, P.W.O., Schaltegger, U., 2003. The composition of zircon and igeous and metamorphic petrogenesis. In: Hanchar, J.M., Hoskin, P.W.O. (Eds.), Ziron, Reviews in Mineralogy and Geochemistry, vol. 53. Mineralogical Society of America, pp. 27–55.

Ivanov, R., 1981. The deep-seated Central-Rhodope Nappe and the interference tectonics of the Rhodope crystalline basement. Geologica Balcanica 11 (3), 47–66.

Jercinovic, M.J., Williams, M.L., 2005. Analytical perils (and progress) in electron microprobe trace element analysis applied to geochronology: background acquisition interferences, and beam irradiation effects. American Mineralogist 90, 526–546.

Kilias, A., Mountrakis, D., 1990. Kinematics of the crystalline sequences in the western Rhodope Massif. Geologica Rhodopica 2, 100–116.

Kohn, M.J., Wieland, M.S., Parkinson, C.D., Upreti, B.N., 2005. Five generations of monazite in Lantang gneisses: implications for chronology of the Himalayan metamorphic core. Journal of Metamorphic Geology 23, 399–406.

Krohe, A., Mposkos, E., 2002. Multiple generations of extensional detachments in the Rhodope Mountains (northern Greece): evidence of episodic exhumation of high-pressure rocks. In: Blundell, D.J., Neubauer, F., von Quadt, A. (Eds.), The Timing and Location of Major Ore Deposits in an Evolving Orogen. Spec. Publ., vol. 204. Geol. Soc., London, pp. 151–178.

Liati, A., 1986. Regional Metamorphism and Overprinting Contact Metamorphism of the Rhodope Zone, Near Xanthi (N. Greece). PhD Thesis, Univ. Carolo-Wilhelmina, Braunschweig, Germany, 186 pp.

Liati, A., 2005. Identification of repeated Alpine (ultra) high-pressure metamorphic events by U–Pb SHRIMP geochronology and REE geochemistry of zircon: the Rhodope zone of Northern Greece. Contribution to Mineralogy and Petrology 150, 608–630.

Liati, A., Gebauer, D., 1999. Constraining the prograde and retrograde P–T–t path of Eocene HP rocks by SHRIMP dating of different zircon domains: inferred rates of heating, burial, cooling and exhumation for central Rhodope, northern Greece. Contribution to Mineralogy and Petrology 135, 340–354.

McFarlane, C.R.M., McCulloch, M.T., 2007. Coupling of in-situ Sm–Nd systematics and U–Pb dating of monazite and allanite with applications to crustal evolution studies. Chemical geology 245, 45–60.

McFarlane, C.R.M., Connely, J.N., Carlson, W.D., 2006. Contrasting response of monazite and zircon to a high-T thermal overprint. Lithos 88, 135–149.

Matthews, A., Liati, A., Mposkos, E., Skarpelis, N., 1996. Oxygen isotope geochemistry of the Rhodope polymetamorphic terrain in northern Greece: evidence for preservation of pre-metamorphic isotopic compositions. European Journal of Mineralogy 8, 1139–1152.

Matthews, A., Putlitz, B., Hamiel, Y., Hervig, R.L., 2003. Volatile transport during the crystallization of anatectic melts: oxygen, boron and hydrogen stable isotope study on the metamorphic complex of Naxos, Greece (2003). Geochimica et Cosmochimica Acta 67, 6145–6163.

Montel, J.M., Foret, S., Veschambre, M., Nicollet, Provost, A., 1996. Electron microprobe dating of monazite. Chemical Geology 131, 37–53.

Mposkos, E., Kostopoulos, D., 2001. Diamond, former coesite and supersilicic garnet in metasedimentary rocks from the Greek Rhodope: a new ultrahigh-pressure metamorphic province established. Earth and Planetary Science Letters 192, 497–506.

Papanikolaou, D., Panagopoulos, A., 1981. On the structural style of Southern Rhodope, Greece. Geologica Balcanica 11 (3), 13–22.

Paquette, J.L., Tiepolo, M., 2007. High resolution (5 μm) U–Th–Pb isotope dating of monazite with excimer laser ablation (ELA)-ICP-MS. Chemical Geology 240, 222–237.

Parrish, R., 1990. U–Pb dating of monazite and its application to geological problems. Canadian Journal of Earth Sciences 27, 1431–1450.

Pyle, J.M., Spear, F.S., 2003. Four generations of accessory-phase growth in low-pressure migmatites from SW New Hampshire. American Mineralogist 88, 338–351.

Pyle, J.M., Spear, F.S., Wark, D.A., Daniel, C.G., Storm, L.C., 2005. Contributions to precision and accuracy of chemical ages of monazite. American Mineralogist 90, 547–577.

Perraki, M., Proyer, A., Mposkos, E., Kaindl, R., Hoinkes, G., 2006. Raman micro-spectroscopy on diamond, graphite and other carbon polymorphs from the ultrahigh-pressure metamorphic Kimi Complex of the Rhodope Metamorphic Province, NE Greece. Earth and Planetary Science Letters 241, 672–685.

Poitrasson, F., Chenery, S., Bland, D.J., 1996. Contrasted monazite hydrothermal alteration mechanisms and their geochemical implications. Earth and Planetary Science Letters 145, 79–96.

Poitrasson, F., Chenery, S., Shepherd, T.J., 2000. Electron microprobe and LA-ICP-MS study of monazite hydrothermal alteration: implications for U–Th–Pb geochronology and nuclear ceramics. Geochimica et Cosmochimica Acta 64, 3283–3297.

Rasmussen, B., Muhling, J.R., 2007. Monazite begest monazite: evidence for dissolution of detrital monazite and reprecipitation of syntectonic monazite during low-grade regional metamorphism. Contribution to Mineralogy and Petrology 154, 675–689.

Rasmussen, B., Muhling, J.R., Fletcher, I.R., Wingate, M.T.D., 2006. In situ SHRIMP U–Pb dating of monazite integrated with petrology and textures: does bulk composition control whether monazite forms in low-Ca pelitic rocks during amphibolite facies metamorphism? Geochimica et Cosmochimica Acta 70, 3040–3058.

Reischmann, T., Kostopoulos, D., 2002. Timing of UHPM in metasediments from the Rhodope Massif, N Greece. Proceedings Goldschmidt Conf., Davos, Switzerland, p. 634.

Renne, P.R., Swisher, C.C., Deino, A.L., Karner, D.B., Owens, T.L., DePaolo, D.J., 1998. Intercalibration of standards, absolute ages and uncertainties in $^{40}Ar/^{39}Ar$ dating. Chemical Geology 145, 117–152.

Ricou, L.E., Burg, J.P., Godfriaux, I., Ivanov, Z., 1998. Rhodope and Vardar: the metamorphic and the olistostromic paired belts related to the Cretaceous subduction under Europe. Geodinamica Acta 11, 285–309.

Rogers, J.J.W., Adams, J.A.S., 1969. Thorium behavior during weathering and rock alteration. In: Wedepohl, K.H., Correns, C.W., Shaw, D.M., Turekian, K.K., Zemann, J. (Eds.), Handbook of geochemistry, vol. II-5. Springer-Verlag, p. 90-G-1.

Ruffet, G., Féraud, G., Amouric, M., 1991. Comparison of ^{40}Ar– ^{39}Ar conventional and laser dating of biotites from the North Trégor Batholith. Geochimica et Cosmochimica Acta 55, 1675–1688.

Ruffet, G., Féraud, G., Ballèvre, M., Kiénast, J.-R., 1995. Plateau ages and excess argon in phengites: an ^{40}Ar– ^{39}Ar laser probe study of Alpine micas (Sesia Zone, Western Alps, northern Italy). Chemical Geology (Isotopic Geoscience Section) 121, 327–343.

Schärer, U., 1984. The effect of initial ^{230}Th disequilibrium on young U–Pb ages: the Makalu case, Himalaya. Earth and Planetary Sciences 67, 191–204.

Seydoux-Guillaume, A.M., Paquette, J.L., Wiedenbeck, M., Montel, J.M., Heinrich, W., 2002. Experimental resetting of the U–Th–Pb systems in monazite. Chemical Geology 191, 165–181.

Seydoux-Guillaume, A.M., Goncalves, P., Wirth, R., Deutsch, A., 2003. Transmission electron microscope study of polyphase and discordant monazites; site-specific specimen preparation using the focused ion beam technique. Geology 31, 973–976.

Simpson, C., 1985. Deformation of granitic rocks across the brittle–ductile transition. Journal of Structural Geology 7, 503–511.
Smith, H.A., Giletti, B.J., 1997. Lead diffusion in monazite. Geochimica and Cosmochimica Acta 61, 1047–1055.
Spear, F.S., Pyle, J.M., 2002. Apatite, monazite and xenotime in metamorphic rocks. In: Kohn, J., Rakovan, J., Hughes, J.M. (Eds.), Phosphates, Geochemical, Geobiological, and Materials Importance. Reviews in Mineralogy and Geochemistry, vol. 48. Mineralogical Society of America, pp. 293–335.
Taylor, B.E., Foord, E.E., Friedrichsen, H., 1979. Stable isotope and fluid inclusion studies of GEM-bearing granitic–pegmatite–aplite dikes, San Diego Co, California. Contribution to Mineralogy and Petrology 68, 187–205.
Teufel, S., Heinrich, W., 1997. Partial resetting of the U–Pb isotope system in monazite through hydrothermal experiments: an SEM and U–Pb isotope study. Chemical Geology 137, 273–281.
Tiepolo, M., 2003. In situ Pb geochronology of zircon with laser ablation-inductively coupled plasma-sector field mass spectrometry. Chemical Geology 199, 159–177.
Townsend, K.J., Miller, C.F., D'Andrea, J.L., Ayers, J.C., Harrison, T.M., Coath, C.D., 2000. Low temperature replacement of monazite in the Ireteba granite, Southern Nevada: geochronological implications. Chemical Geology 172, 95–112.
Turpaud, P., 2006. Characterization of Igneous Terranes by Zircon Dating: Implications for the UHP Relicts Occurrences and Suture Identification in the Central Rhodope, Northern Greece. PhD Thesis, Univ. Johannes Gutenberg, Mainz, Germany, 107 pp.
van Achterbergh, E., Ryan, C.G., Jackson, S.E., Griffin, W., 2001. Data reduction software for LA-ICP-MS. In: Sylvester, P. (Ed.), Laser ablation-ICP-MS in the Earth Science. Mineralogical Association of Canada, 29, pp. 239–243.
Wiedenbeck, M., Allé, P., Corfu, F., Griffin, W.L., Meier, M., Oberli, F., von Quadt, A., Roddick, J.C., Spiegel, W., 1995. Three natural zircon standards for U–Th–Pb, Lu–Hf, trace-elements and REE analyses. Geostandard Newsletter 19, 1–23.
Williams, M.L., Jercinovic, M.J., Goncalves, P., Mahan, K.H., 2006. Format and philosophy for collecting, compiling, and reporting microprobe monazite ages. Chemical Geology 225, 1–15.
Williams, M.L., Jercinovic, M.J., Hetherington, C.J., 2007. Microprobe monazite geochronology: understanding geologic processes by integrating composition and chronology. Annual Review of Earth and Planetary Sciences 35, 137–175.
Zachos, S., Dimadis, E., 1983. The geotectonic position of the Skaloti–Echinos granite and its relationship to the metamorphic formations of Greek Western and Central Rhodope. Geologica Balcanica 13 (5), 17–24.
Zheng, Y.F., 1993. Calculation of oxygen isotope fractionation in anhydrous silicate minerals. Geochimica et Cosmochimica Acta, 57, 1079–1091.
Zhu, X.K., O'Nions, R.K., 1999a. Zonation of monazite in metamorphic rocks and its imlications for high temperature thermochronology: a case study from the Lewisian terrain. Earth and Planetary Sciences 171, 209–220.
Zhu, X.K., O'Nions, R.K., 1999b. Monazite chemical composition: some implications for monazite geochronology. Contribution to Mineralogy and Petrology 137, 351–363.